

Ongoing star formation in the proto-cluster IRAS 22134+5834

Yuan Wang (王渊)^{1,2}, Marc Audard¹, Francesco Fontani³, Álvaro Sánchez-Monge⁴, Gemma Busquet^{5,6}, Aina Palau⁷, Henrik Beuther⁸, Jonathan C. Tan⁹, Robert Estalella¹⁰, Andrea Isella¹¹, Frederic Gueth¹², and Izaskun Jiménez-Serra¹³

¹ Department of Astronomy, University of Geneva, Chemin d'Ecogia 16, CH-1290 Versoix, Switzerland
e-mail: yuan.wang@unige.ch

² Purple Mountain Observatory, Chinese Academy of Sciences, 2 West Beijing Road, 210008 Nanjing, P.R. China

³ INAF – Osservatorio Astrofisico di Arcetri, L.go E. Fermi 5, 50125 Firenze, Italy

⁴ I. Physikalisches Institut, Universität zu Köln, Zùlpicher Str. 77, 50937, Cologne, Germany

⁵ Insitut de Ciències de l' Espai (CSIC-IIEEC), Campus UAB, carrer de Can Magran S/N 08193, Cerdanyola del Vallès, Catalunya, Spain

⁶ Instituto de Astrofísica de Andalucía, CSIC, Glorieta de la Astronomía, s/n E-18008 Granada, Spain

⁷ Instituto de Radioastronomía y Astrofísica, Universidad Nacional Autónoma de México, P.O. Box 3-72, 58090, Morelia, Michoacán, Mexico

⁸ Max-Planck-Institut für Astronomie, Königstuhl 17, D-69117, Heidelberg, Germany

⁹ Departments of Astronomy and Physics, University of Florida, Gainesville, FL 32611, USA

¹⁰ Dept. d'Astronomia i Meteorologia, Institut de Ciències del Cosmos, Univ. de Barcelona, IEEC-UB, Martí Franques 1, E08028 Barcelona, Spain

¹¹ Department of Physics & Astronomy - MS 108, Rice University, 6100 Main Street, Houston, TX, 77005, USA

¹² Institut de Radioastronomie Millimétrique (IRAM), 300 rue de la Piscine, 38406 Saint Martin d' Hères, France

¹³ University College London, Department of Physics and Astronomy, 132 Hampstead Road, London NW1 2PS, UK

Received May 2015; accepted Oct. 2015

ABSTRACT

Aims. Massive stars form in clusters, and their influence on nearby starless cores is still poorly understood. The protocluster associated with IRAS 22134+5834 represents an excellent laboratory to study the influence of massive YSOs on nearby starless cores, and the possible implications in the clustered star formation process.

Methods. IRAS 22134+5834 was observed in the centimeter with (E)VLA, 3 mm with CARMA, 2 mm with PdBI, and 1.3 mm with SMA, to study the continuum emission as well as the molecular lines, that trace different physical conditions of the gas.

Results. The multi-wavelength centimeter continuum observations revealed two radio sources within the cluster, VLA1 and VLA2. VLA1 is considered to be an optically thin UCH_{II} region with a size of 0.01 pc and sits at the edge of the near-infrared (NIR) cluster. The flux of ionizing photons of the VLA1 corresponds to a B1 ZAMS star. VLA2 is associated with an infrared point source and has a negative spectral index. We resolved six millimeter continuum cores at 2 mm, MM2 is associated with the UCH_{II} region VLA1, and other dense cores are distributed around the UCH_{II} region. Two high-mass starless clumps (HMSC), HMSC-E (east) and HMSC-W (west), are detected around the NIR cluster with N₂H⁺(1–0) and NH₃ emission, and show different physical and chemical properties. Two N₂D⁺ cores are detected on an NH₃ filament close to the UCH_{II} region, with a projected separation of ~8000 AU at the assumed distance of 2.6 kpc. The kinematic properties of the molecular line emission confirm the expansion of the UCH_{II} region and that the molecular cloud around the near infrared (NIR) cluster is also expanding.

Conclusions. Our multi-wavelength study has revealed different generations of star formation in IRAS 22134+5834. The formed intermediate- to massive stars show strong impact on nearby starless clumps. We propose that while the stellar wind from the UCH_{II} region and the NIR cluster drives the large scale bubble, the starless clumps and HMPOs formed at the edge of the cluster.

Key words. stars: formation – stars: massive – ISM: molecules – ISM: bubbles – ISM: individual objects: IRAS 22134+5834

1. Introduction

Despite the fact that most stars in our Galaxy form in rich clusters (e.g., Lada & Lada 2003), the initial conditions of clustered star formation are still poorly understood. Studies of low-mass pre-stellar cores in low-mass star forming regions suggest that cluster environments have a relatively small influence on the properties of the cores (i.e., temperature, mass, velocity dispersion, and chemical abundance, e.g., André et al. 2007; Friesen et al. 2009; Foster et al. 2009). However, these conclusions likely do not apply to high-mass star forming regions. Previous high-angular resolution observations have revealed that high-mass sources with different evolutionary stages, from pre-stellar cores to ultra-compact H_{II} (UCH_{II}) regions, coexist in the same star-forming complex close to each other, and the age spread within the cluster members could be as large as ~ 2 to 3 Myr (e.g., Bik et al. 2012; Wang et al. 2011; Palau et al. 2010). The strong ultraviolet (UV) radiation, massive outflows from the newly formed high-mass stars, or expanding H_{II} regions can have a strong impact on the environment around high-mass pre-stellar cores detected interferometrically in dense gas tracers (e.g., N₂H⁺, NH₃, Palau et al. 2010; Sánchez-Monge et al. 2013).

Previous studies show that these energetic phenomena could have major effects on pre-stellar dense cores. Millimeter interferometer observations performed by Palau et al. (2007b) detected several pre-stellar candidates compressed by the expanding cavity driven by a massive young stellar objects (YSO) in IRAS 20343+4129, and the line widths are clearly non-thermal, contrary to what is observed in clustered low-mass pre-stellar cores. In the protocluster associated with IRAS 05345+3157 Fontani et al. (2009) found that the kinematics of two pre-stellar core candidates are influenced by the passage of a massive outflow; Palau et al. (2007a) found that in IRAS 20293+3952 the UV radiation and outflows can also affect the chemistry of starless cores, but the deuteration of species like N₂H⁺ and NH₃, seems to remain as high as in pre-stellar cores associated with low-mass star forming regions (Fontani et al. 2008, 2009; Busquet et al. 2010; Germer et al. 2015). However, the aforementioned regions have $L_{\text{bol}} \lesssim 5,000 L_{\odot}$, and the effects of a higher-mass protostar on its surroundings, both at small (< 5000 AU) and large scales ($> 10,000$ AU), remain poorly constrained from an observational point of view. On the other hand, a NIR photometry and spectroscopy towards the high-mass star forming region RCW 34 (Bik et al. 2010) suggests that the low- and intermediate-mass stars formed first and produced the “bubble”, while the O star formed later at the edge and induces the formation of the next generation stars in the molecular cloud.

Situated at a distance of 2.6 kpc, IRAS 22134+5834 (hereafter I22134) has a luminosity of $1.2 \times 10^4 L_{\odot}$ and is associated with a centimeter compact source of a few mJy (Sridharan et al. 2002). At millimeter wavelengths, this region is dominated by an extended continuum source which peaks on the IRAS source (Chini et al. 2001; Beuther et al. 2002b). A massive molecular outflow is also detected with single-dish telescopes in CO (Dobashi et al. 1994; Dobashi & Uehara 2001; Beuther et al. 2002b) and HCO⁺(1–0) (López-Sepulcre et al. 2010), which indicates one or more high-mass stars are forming. NIR *K*-band images reveal a ring-shaped embedded cluster made of early- to late-B type young stars with a central dark region (Kumar et al. 2003). Furthermore, multiple starless cores are found around the centimeter source and the NIR cluster (Busquet 2010; Sánchez-Monge 2011; Sánchez-Monge et al. 2013). Therefore, the protocluster associated with I22134 represents an excellent laboratory

to study the influence of massive YSOs on nearby starless dense cores.

In this paper we investigate the properties of the dense cores in I22134, and the relations between with the ambient molecular clouds and the more evolved cluster members. In Sect. 2 we describe the observations and data reduction. In Sect. 3 we present the millimeter and centimeter continuum results, and the properties of the starless clumps from molecular line observations. We discuss properties of the sources and interactions between the YSOs and the molecular cloud in Sect. 4 and summarize the main conclusions in Sect. 5

2. Observations and data reduction

We observed the star-forming region I22134 with the (Expanded) Very Large Array (VLA¹), the Combined Array for Research in Millimeter-wave Astronomy (CARMA²), the Plateau de Bure Interferometer (PdBI) and the Submillimeter Array (SMA³). Table 1 and 2 summarise the observations.

2.1. (E)VLA

The I22134 star-forming region was observed with the VLA at 6.0, 3.6, 1.3, and 0.7 cm wavelengths in the A, B, and C configurations of the array, in 2007 and 2009, with 10-21 EVLA antennas in the array. The data reduction followed the VLA standard guidelines for calibration of high frequency data, using the NRAO package AIPS. We complemented our continuum observations with 1.4 GHz continuum archival data from the NRAO VLA Sky Survey (NVSS) (Condon et al. 1998). We list the main parameters of the observations in Table 1.

The EVLA was also used on April 23 and May 07, 2010 to observe the continuum emission at 6.0 and 3.6 cm in its D configuration, with a bandwidth of 2×256 MHz (up to 5 times better than the standard VLA observations). The data reduction followed the EVLA standard guidelines for continuum emission, using the Common Astronomy Software Applications package (CASA). Images were done with the CLEAN procedure in CASA with different robust parameters (robust= -5 for the EVLA 6.0 and 3.6 cm data, and $=0$ for the rest of the images), the resulting rms noise levels and synthesized beams are shown in Table 1.

The NH₃ (*J, K*) = (1, 1) and (2, 2) inversion lines (project AK558) were obtained during 2003 May 01 in its D configuration with the VLA. The phase center was R.A. 22^h15^m08^s.099 Dec. +58°49′10″00 (J2000). Amplitude and phase calibration were achieved by regularly interleaved observations of the quasar 2148+611. The bandpass was calibrated by observing the bright quasars 1229+020 (3C273) and 0319+415 (3C84). The

¹ The Very Large Array (VLA) is operated by the National Radio Astronomy Observatory (NRAO), a facility of the National Science Foundation operated under cooperative agreement by Associated Universities, Inc.

² Supports for CARMA construction were derived from the Gordon and Betty Moore Foundation, the Kenneth T. and Eileen L. Norris Foundation, the Associates of the California Institute of Technology, the states of California, Illinois, and Maryland, and the National Science Foundation. Ongoing CARMA development and operations are supported by the National Science Foundation under a cooperative agreement, and by the CARMA partner universities.

³ The Submillimeter Array is a joint project between the Smithsonian Astrophysical Observatory and the Academia Sinica Institute of Astronomy and Astrophysics and is funded by the Smithsonian Institution and the Academia Sinica.

absolute flux scale was set by observing the quasar 1331+305 (3C286), and we adopted a flux of 2.41 Jy at the frequencies of 23.69 and 23.72 GHz. The 4IF spectral line mode was used to observe simultaneously the $\text{NH}_3(1, 1)$ and $(2, 2)$ lines with two polarizations. The bandwidth was 3.1 MHz, with 128 channels with a channel spacing of 24.2 kHz ($\sim 0.3 \text{ km s}^{-1}$) centred at $v_{\text{LSR}} = -18.3 \text{ km s}^{-1}$. The data reduction was done with the software package AIPS following the standard guidelines for calibration of high frequency data. Imaging was performed using natural weighting, the resulting rms and synthesized beams are listed in Table 3. The same data were also presented in Sánchez-Monge et al. (2013).

2.2. CARMA

CARMA was used to observe the 3 mm continuum and the selected molecular lines towards I22134 in the D configuration with 14 antennas (five 10.4 m antennas and nine 6 m antennas) in two different runs carried out on June 23, 2008 and May 4, 2010. During the first run we covered the $\text{N}_2\text{H}^+(1-0)$ transition. The phase center was R.A. $22^{\text{h}}15^{\text{m}}09^{\text{s}}23$ Dec. $+58^{\circ}49'08''9$ (J2000), and the baseline ranged from 10 to 108 m. The Full Width at Half Maximum (FWHM) of the primary beam at 93 GHz was $132''$ for the 6 m antennas, and $77''$ for the 10.4 m antennas. The system temperatures were around 200 K during the observations. All the hyperfine transitions of $\text{N}_2\text{H}^+(1-0)$ were covered with two overlapping 8 MHz units, with 63 channels of each unit, resulting in a velocity resolution of $\sim 0.42 \text{ km s}^{-1}$. Amplitude and phase calibration were achieved by regularly interleaved observations of BL Lac. The bandpass was calibrated by observing the brightest quasar 3C454.3. The absolute flux scale was set by observing MWC349, with an estimated uncertainty around 20%. The observations carried out on 2010 were obtained with the new CARMA correlator, which provides up to 8 bands. The phase center was R.A. $22^{\text{h}}15^{\text{m}}08^{\text{s}}1$ Dec. $+58^{\circ}49'10''0$ (J2000), and the baseline ranged from 9 to 95 m. We used three 500 MHz bands to observe the continuum and five bands were set up to observe the $\text{C}_2\text{H}(N=1-0)$, $\text{CH}_3\text{OH}(2_{0,2} - 1_{0,1})\text{A}+$ (together with $\text{CH}_3\text{OH}(2_{-1,2} - 1_{-1,1})\text{E}$), $\text{HCO}^+(1-0)$, *ortho*- $\text{NH}_2\text{D}(1_{1,1} - 1_{0,1})$, $\text{CCS}(7_6 - 6_5)$ and *c*- $\text{C}_3\text{H}_2(2_{1,2} - 1_{0,1})$ line emission. Amplitude and phase calibration were achieved by regularly interleaved observations of the nearby quasar 2038+513. The bandpass was calibrated by observing 3C454.3, flux calibration was set by observing Neptune. The estimated uncertainty of the absolute flux calibration is about $\sim 10 - 15\%$.

Data calibration and imaging (natural weighting) were conducted in MIRIAD (Sault et al. 1995). The resulting synthesized beam and rms for the continuum and detected molecular lines are listed in Table 2 and Table 3, respectively. We did not detect emission from $\text{HCO}^+(1-0)$, $\text{CCS}(7_6 - 6_5)$ and *c*- $\text{C}_3\text{H}_2(2_{1,2} - 1_{0,1})$ at the 3σ limit of $130 \text{ mJy beam}^{-1}$ with a velocity resolution of 0.4 km s^{-1} , hence we do not discuss these data in this paper.

2.3. PdBI

Observations in the 2 mm continuum and the $\text{N}_2\text{D}^+(2-1)$ line at 154.217 GHz were obtained on June 02 and November 28, 2010, with the PdBI in the D and C configurations, respectively. The phase centre was R.A. $22^{\text{h}}15^{\text{m}}10^{\text{s}}.00$ Dec. $+58^{\circ}49'02''6$ (J2000). Baselines range from $\sim 19-178$ m. Atmospheric phase corrections were applied to the data, and the averaged atmospheric precipitable water vapor was ~ 5 mm. The bandpass calibration was carried out using 1749+096. Calibration of phase and amplitude

of the complex gains were made by observing the nearby quasars 2146+608 and 2037+511. The phase rms is 10° to 40° , and the amplitude rms is below 10%. The adopted flux density for the flux calibrator, MWC349, was 1.45 Jy. Calibration and imaging (natural weighting for $\text{N}_2\text{D}^+(2-1)$ and *robust*=-2 for the continuum) were performed using the CLIC and MAPPING softwares of the GILDAS⁴ package using standard procedures. The resulting synthesized beam and rms for the continuum and molecular lines are listed in Table 2 and 3, respectively.

2.4. SMA

I22134 was observed with the SMA on September 28, 2010 in the extended configuration with eight antennas (baselines range $\sim 21-180$ m). The phase center of the observations is R.A. $22^{\text{h}}15^{\text{m}}10^{\text{s}}.00$ Dec. $+58^{\circ}49'02''6$ (J2000), and the local standard of rest velocity was assumed to be $=-18.3 \text{ km s}^{-1}$. The SMA has two sidebands separated by 10 GHz. The correlator was set to 2 GHz mode, and the receivers were tuned to 231.321 GHz in the upper sideband and a uniform velocity resolution of $\sim 0.6 \text{ km s}^{-1}$. The system temperatures were around $\sim 100-200$ K during the observations (zenith opacities $\tau_{225 \text{ GHz}} \lesssim 0.08$ as measured by the Caltech Submillimeter Observatory). Bandpass was derived from the quasar 3C84 observations. Phase and amplitude were calibrated with regularly interleaved observations of quasars BL Lac and 3C418. The flux calibration was derived from BL Lac observations, and the flux scale is estimated to be accurate within 20%. We applied different robust parameters for the continuum and line data (*robust*=1 for the continuum, and 2 for the line images), the resulting synthesized beam and rms for the continuum and molecular lines are listed in Table 2 and 3, respectively. Besides the $\text{SO}(6_5 - 5_4)$ and $\text{CO}(2-1)$, the two isotopologues of CO (^{13}CO and C^{18}O) are also detected, however, the emission of these two transitions suffers severe missing flux problem, and we do not discuss these data in this paper. The flagging and calibration were done with the IDL superset MIR (Scoville et al. 1993), which was originally developed for the Owens Valley Radio Observatory and adapted for the SMA⁵. The imaging and data analysis were conducted in MIRIAD (Sault et al. 1995).

3. Results

3.1. Centimeter continuum emission

VLA radio continuum emission is detected towards I22134 at all wavelengths (Fig. 1). At low angular resolution ($6'' - 14''$) the 6 cm and 3.6 cm emission is dominated by a strong and compact source VLA1, which is associated with one of the strongest IRAC sources in the field at $3.6 \mu\text{m}$ and is saturated at longer wavelengths in the IRAC band. A secondary radio source VLA2 is located $\sim 15''$ to the northwest of VLA1, and is also associated with a B star (Kumar et al. 2003). Only VLA1 is detected in the high angular resolution observations ($\lesssim 1''$, bottom panels in Fig. 1), and at 3.6 cm and 1.3 cm it is resolved into a cometary morphology with the head of the cometary arc pointing towards the southeast. The peak intensity and flux density measurements of VLA1 and VLA2 are listed in Table 4. The flux

⁴ The GILDAS software is developed at the IRAM and the Observatoire de Grenoble, and is available at <http://www.iram.fr/IRAMFR/GILDAS>.

⁵ The MIR cookbook by Chunhua Qi can be found at <http://cfa-www.harvard.edu/~cqi/mircook.html>.

Table 1. (E)VLA continuum observational parameters .

λ (cm)	Project ID.	Config.	Epoch	Bootstr. Flux of Gain cal. 2148+611 ^a	Flux cal.	Beam ("×")	P.A. (°)	rms (μ Jy beam ⁻¹)
VLA								
20.0	NVSS ^b	D	1995 Mar. 12	45.×45	0	470
6.0	AS902	A	2007 Jun. 05	1.28±1%	3C286	0.41×0.36	-17	37
3.6	AS902	A	2007 Jun. 05	1.05±1%	3C286	0.24×0.19	+25	17
1.3	AB1274	B	2007 Oct. 23	0.72±3%	3C286	0.30×0.22	+31	64
0.7	AS981	C	2009 Jun. 28	0.68±5%	3C286	0.63×0.39	+68	180
EVLA								
6.0	AS1038	D	2010 Apr 23	1.29±1%	3C48	14.3×10.0	+33	26
3.6	AS1038	D	2010 May 07	1.02±1%	3C48	8.3×5.9	+44	27

Notes. ^(a) Bootstrapped flux is in Jy.

^(b) The detailed description for NVSS data can be found in Condon et al. (1998).

Table 2. Millimeter continuum observational parameters .

Array	λ (mm)	Config.	Epoch	Gain cal.	Bandpass cal.	Flux cal.	Beam* ("×")	P.A.* (°)	rms* (mJy beam ⁻¹)
CARMA	3	D	2008 Jun. 12	BL Lac	3C454.3	MWC349	7.15×5.71	+23	0.38
CARMA	3	D	2010 May 04	2038+513	3C454.3	Neptune	7.15×5.71	+23	0.38
PdBI	2	D	2010 Jun. 02	2146+608, 2037+511	1749+096	MWC349	2.67×1.58	+89	0.26
PdBI	2	C	2010 Nov. 28	2146+608, 2037+511	1749+096	MWC349	2.67×1.58	+89	0.26
SMA	1.3	Extended	2010 Sep. 28	BL Lac, 3C418	3C84	BL Lac	1.26×1.00	-87	0.50

Notes. ^(*) The beam size and rms listed here for CARMA and PdBI observations are derived by combining the data from both configurations.

Table 3. Molecular line observation parameters.

Lines	Frequency ^a (GHz)	Telescope	Config.	Beam ("×")	PA (°)	Velocity resol. (km s ⁻¹)	rms ^b (mJy beam ⁻¹)
NH ₃ (1, 1)	23.694500	VLA	D	3.77 × 3.10	+89	0.3	1.2
NH ₃ (2, 2)	23.722630	VLA	D	3.69 × 3.00	+84	0.3	1.2
N ₂ H ⁺ (1-0)	93.176254	CARMA	D	5.49 × 4.09	-82	0.4	31
C ₂ H(N=1-0)	87.316898	CARMA	D	6.49 × 5.23	+22	0.4	50
CH ₃ OH(2 _{-1,2} - 1 _{-1,1})E	96.739362	CARMA	D	6.03 × 4.79	+27	0.06	108
CH ₃ OH(2 _{0,2} - 1 _{0,1})A+	96.741375	CARMA	D	6.03 × 4.79	+27	0.06	108
<i>ortho</i> -NH ₂ D(1 _{1,1} - 1 _{0,1})	85.926278	CARMA	D	6.79 × 5.40	+27	0.07	91
N ₂ D ⁺ (2-1)	154.217011	PdBI	C+D	2.96 × 1.94	+94	0.3	6.0
CO(2-1)	230.538000	SMA	Extended	1.41 × 1.02	-88	0.6	36
SO(6 ₅ - 5 ₄)	219.949442	SMA	Extended	1.49 × 1.07	-88	0.6	34

Notes. ^(a) The frequencies for the lines are obtained from the Cologne Database for Molecular Spectroscopy (CDMS, Müller et al. 2001, 2005), except for NH₃ lines that the frequencies are obtained from the JPL Molecular Spectroscopy database (Pickett et al. 1998).

^(b) The rms listed here is per channel.

density of VLA1 is almost constant at all the VLA observations, while VLA2 shows a negative spectral index.

In order to investigate the physical properties of VLA1, we reproduced the VLA images considering only the common uv -range (15–450 k λ) and convolved the resulting images to the same circular beam of 0''.7×0''.7. The measured flux density and the deconvolved size of the continuum source VLA1 obtained for the images with the same uv -range are listed in Table 5 (see also Sánchez-Monge 2011). Figure 2 shows the spectral energy distribution (SED) of the radio source VLA1. The flux of the source remains basically constant at centimeter wavelengths, with a spectral index $\alpha = -0.19$ ($S_\nu \propto \nu^\alpha$) between 6 and 0.7 cm (Fig. 2). Combining the 20 cm data, we can fit the SED with a homogeneous optically thin H α region with a size of 0.01 pc, an electron density (n_e) of 5.5×10^4 cm⁻³, an emis-

sion measure (EM) of 1.0×10^7 cm⁻⁶ pc, an ionized gas mass of $9.1 \times 10^{-5} M_\odot$, and an ionizing photons flux of 2.5×10^{45} s⁻¹ (corresponding to a B1 ZAMS star, Panagia 1973). The size of VLA1 suggests that it could be a hyper-compact H α (HCH α) region, however, HCH α regions should have EM $\sim 1.0 \times 10^{10}$ cm⁻⁶ pc or $n_e \sim 5.5 \times 10^6$ cm⁻³ which means the emission is typically optically thick at cm wavelengths (spectral index $\alpha = 2$, Kurtz 2005; Churchwell 2002), thus VLA1 is considered as a typical UCH α region. Note that these definitions of HCH α and UCH α used here differ from those of Beuther et al. (2007) and Tan et al. (2014), where HCH α s are defined primarily based on size, i.e., as being <0.01pc in diameter, and similarly UCH α s as being <0.1pc in diameter. It is worth noticing that at 20 cm we did not exclude the emission of VLA2, so the fitting result is derived with a 20 cm flux that could be overestimated. As shown in Ta-

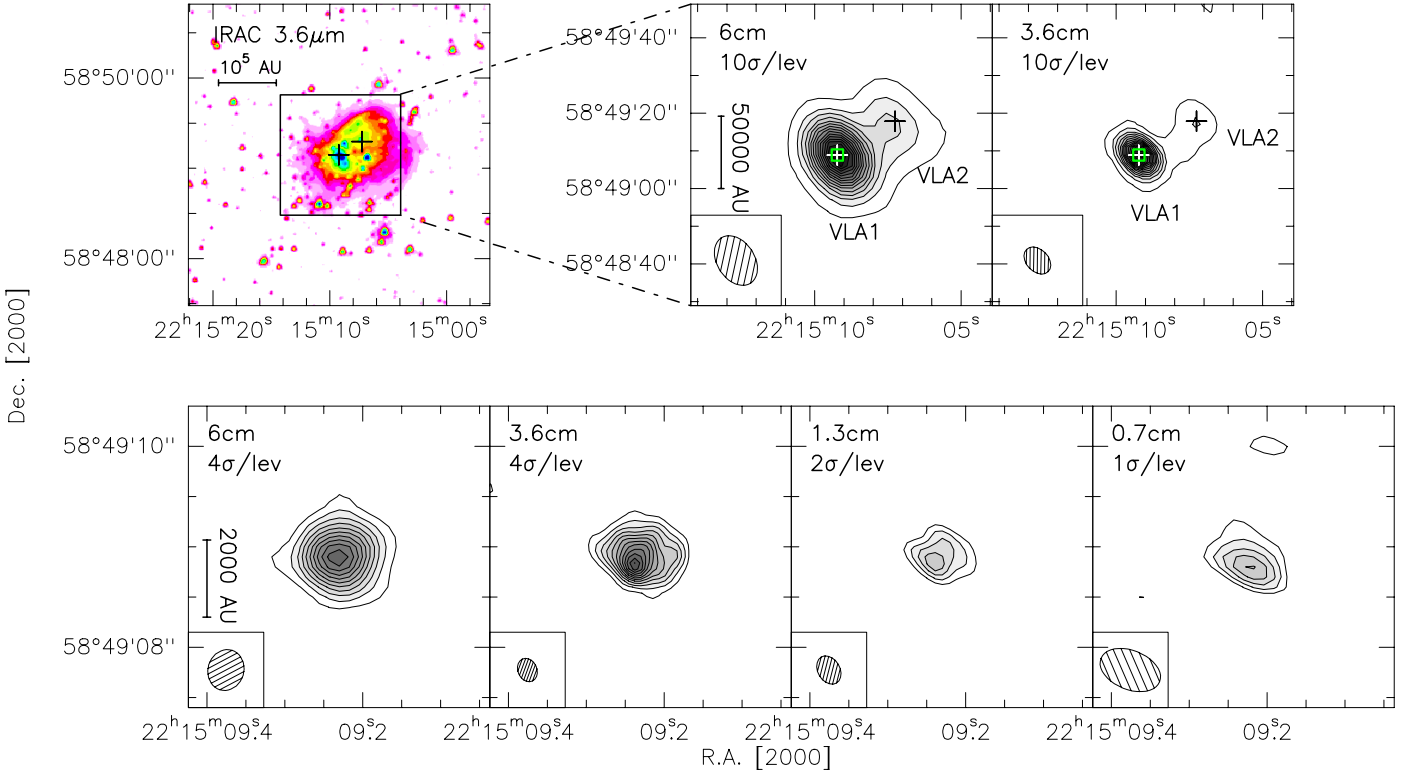


Fig. 1. The *Spitzer*/IRAC and (E)VLA continuum emission images. *Top:* *Spitzer*/IRAC 3.6 μm , ELVA (D-config) 6.0 cm and 3.6 cm continuum images. *Bottom:* The VLA 6.0 cm (A-config), 3.6 cm (A-config), 1.3 cm (B-config), and 0.7 cm (C-config) continuum images. The boxes in the EVLA continuum images in the top mark the region zoomed in bottom panels. All the contour levels start at 4σ , and the steps are shown in each panel. The σ values are listed in Table 4. The crosses in the top-panels mark the two radio sources we detected. The synthesized beams are shown in the bottom left corner of each panel. The *Spitzer*/IRAC post-bcd data processed with pipeline version S18.25.0 have been downloaded from the *Spitzer* archive to create the image.

Table 4. Centimeter continuum properties of VLA1 and VLA2.

λ (cm)	Beam ("×")	P.A. ($^\circ$)	I_ν (mJy beam $^{-1}$)	S_ν (mJy)
VLA1 22:15:09.23 +58:49:08.9 (J2000)				
20.0	45×45	0	1.3±0.47	2.9±0.70
6.0	14.3×10.0	+33	4.2±0.03	4.6±0.08
6.0	0.41×0.36	-17	1.6±0.03	3.5±0.11
3.6	8.3×5.9	+44	3.6±0.02	4.1±0.08
3.6	0.24×0.19	+25	0.8±0.02	3.5±0.09
1.3	0.30×0.22	+31	0.8±0.06	2.1±0.20
0.7	0.63×0.39	+68	1.5±0.18	2.1±0.36
VLA2 22:15:07.26 +58:49:17.9 (J2000)				
6.0	14.3×10.0	+33	0.7±0.1	0.8±0.05
3.6	8.3×5.9	+44	0.4±0.1	0.6±0.06

Notes. ^(*) Error in intensity is the rms noise level of the map. Error in flux density is estimated as $\sqrt{(\sigma \sqrt{\theta_{\text{source}}/\theta_{\text{beam}}})^2 + (\sigma_{\text{flux-scale}})^2}$, where θ_{source} is the size of the source which we used to calculate the flux density (outlined by the lowest contour in Fig. 1), θ_{beam} is the size of the synthesized beam, $\sigma_{\text{flux-scale}}$ is the error in the flux scale which takes into account the uncertainty of the calibration and is estimated as $S_\nu \times \% \text{uncertainty}$ (%uncertainty is listed in Table 1).

ble 4, at 3.6 and 6.0 cm the flux of VLA2 is only about 1/6 of VLA 1. If VLA2 shares the similar SED to VLA1 as we shown in Fig. 2, about 1/7 of the total emission at 20 cm might be due to VLA2. If VLA2 keeps the same power law spectral index between 3.6 and 6.0 cm to 20 cm, about 1/2 of the total emission at 20 cm might be due to VLA2. If we remove the potential influence of VLA 2 to the 20 cm flux the fit we obtained did not

change (less than 1%) and the shape of the SED is basically the same.

3.2. Millimeter continuum emission

Figure 3 shows the millimeter continuum maps of I22134 obtained with CARMA (3 mm), PdBI (2 mm) and SMA (1.3 mm),

Table 5. Flux density for VLA1 with the same uv -range and same circular beam of $0''.7 \times 0''.7$.

λ (cm)	I_ν^* (mJy beam $^{-1}$)	S_ν^* (mJy)	Deconv. Size ("' \times '')	P.A. ($^\circ$)
6.0	2.7 ± 0.04	3.6 ± 0.1	$0.48 \times 0.38 \pm 0.05$	80 ± 10
3.6	2.7 ± 0.04	3.5 ± 0.1	$0.44 \times 0.34 \pm 0.05$	80 ± 10
1.3	2.0 ± 0.07	2.5 ± 0.2	$0.44 \times 0.32 \pm 0.1$	85 ± 25
0.7	1.9 ± 0.17	2.8 ± 0.4	$0.62 \times 0.37 \pm 0.3$	85 ± 30

Notes. ^(*) The errors are estimated with the same method described in the note of Table 4.

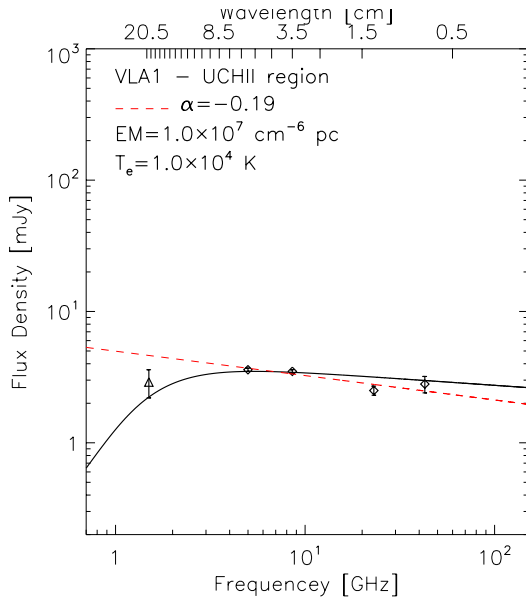


Fig. 2. Spectral energy distribution for radio source VLA1. Diamonds correspond to the VLA high-angular resolution flux measurements listed in Table 5. The triangle corresponds to the 20 cm flux measurement in Table 4. The dashed line shows the linear fit ($S_\nu \propto \nu^\alpha$) to the high-angular resolution data (diamonds) with $\alpha = -0.19$. The solid line shows a homogeneous HII region fit to all the data points in the figure.

and Figure 4 shows the continuum maps overlaid on the UKIRT K -band ($2.2 \mu\text{m}$) and *Spitzer*/IRAC $3.6 \mu\text{m}$ images. At 3 mm, we detected one main millimeter clump with weak extended emission towards the southeast. With much better angular resolution, the clump is resolved into multiple cores at 2 mm and 1.3 mm. In the 3 mm continuum map the size of the clump is outlined by the 3σ contour ($1\sigma = 0.38 \text{ mJy beam}^{-1}$, Fig. 3). For the 2 mm and 1.3 mm continuum maps, we employ the application FINDCLUMPS⁶ Figure 3 shows that the 2 mm core MM1 is associated with one 1.3 mm core, MM3 is resolved

⁶ FINDCLUMPS is a part of the open source software package Starlink, which was a long running UK Project supporting astronomical data processing. It was shut down in 2005 but the software continued to be developed at the Joint Astronomy Centre until March 2015, and is now maintained by the East Asian Observatory. with the algorithm ClumpFind (Williams et al. 1994) and 3σ boundaries ($1\sigma = 0.26 \text{ mJy beam}^{-1}$ for 2 mm and $= 0.50 \text{ mJy beam}^{-1}$ for 1.3 mm continuum map) to identify the cores. The identified cores which are located outside the FWHM of the primary beam ($32''$ for the PdBI, and $55''$ for the SMA) or have a peak intensity less than 5σ are rejected manually. Eventually, we identified 6 cores at 2 mm and 5 at 1.3 mm. The properties of the cores we identified are listed in Table 6. The sizes and fluxes are derived from ClumpFind, the peak intensities and positions are measured from the continuum maps directly.

into two 1.3 mm cores, named MM3a and MM3b. The 2 mm core MM5 is resolved into two cores at 1.3 mm, named MM5a and MM5b. MM2 is associated with one near-infrared source at seen in the K -band image (Fig. 4) and the UCHII region VLA1 (Fig. 1). Figure 4 shows that MM1 coincides with one near-infrared source at K -band. MM3a show no emission at K -band, but strong emission is detected towards this source at longer wavelengths at *Spitzer*/IRAC bands (Fig. 4), which indicates MM3a is still relatively deeply embedded. We do not detect the 1.3 mm counterparts of MM2, MM4 and MM6, which could be due to the 2 mm observations having a better uv -coverage and/or sensitivity than the 1.3 mm observations. If we assume the dust emissivity index of $\beta = 1.8$ and convert the peak intensity of MM2, MM4 and MM6 we measured at 2 mm (Table 6), the results would be above the 3σ detection limit we have with the SMA observations, so the better sensitivity of the PdBI is not the reason we do not detect the 1.3 mm counterparts of these cores. Following the method described in the appendix of Palau et al. (2010), we estimated that the largest structure from the shortest baselines of our observations that our PdBI observations could recover is $\sim 9.5''$, while for the SMA observation it is $\sim 5.7''$. Thus the relatively smooth distributed MM2, MM4 and MM6 were filtered out by the SMA observations. VLA2 is not detected at millimeter wavelengths, probably due to the low sensitivity of our mm observations. The open squares in Fig. 3 mark the continuum cores detected by Palau et al. (2013), and the southwest one is associated with MM1. We will discuss the detailed comparison in Sect. 4.1.

Assuming optically thin dust emission and following Equation 1 and 2 (Hildebrand 1983; Schuller et al. 2009) we estimate the gas mass and peak column density of the continuum sources:

$$M_{\text{gas}} = \frac{R S_\nu d^2}{B_\nu(T_{\text{dust}}) \kappa_\nu} \quad (1)$$

$$N_{\text{H}_2} = \frac{R I_\nu}{B_\nu(T_{\text{dust}}) \Omega \kappa_\nu \mu m_{\text{H}}} \quad (2)$$

where S_ν is the total flux density integrated over the source, I_ν is the peak intensity of the source (Table 6), d is the distance to the source $\sim 2.6 \text{ kpc}$, R is the gas-to-dust ratio ~ 100 , Ω is the beam solid angle, μ is the mean molecular weight of the interstellar medium ~ 2.3 , m_{H} is the mass of a hydrogen atom, B_ν is the Planck function for a dust temperature T_{dust} , and κ_ν is the dust opacity $\sim 0.899 \text{ cm}^2 \text{ g}^{-1}$ at 1.3 mm ($0.41 \text{ cm}^2 \text{ g}^{-1}$ at 2 mm, and $0.18 \text{ cm}^2 \text{ g}^{-1}$ at 3 mm for the thin ice mantles at density of 10^6 cm^{-3} , a dust emissivity index of $\beta = 1.8$, Ossenkopf & Henning 1994). Assuming Local Thermodynamic Equilibrium (LTE), the rotational temperature (T_{rot}) obtained from the NH_3 observations (Sect. 3.4.1) approximates kinetic temperature T_{k} . At the densities of our cores (10^5 cm^{-3}), the dust and gas is well

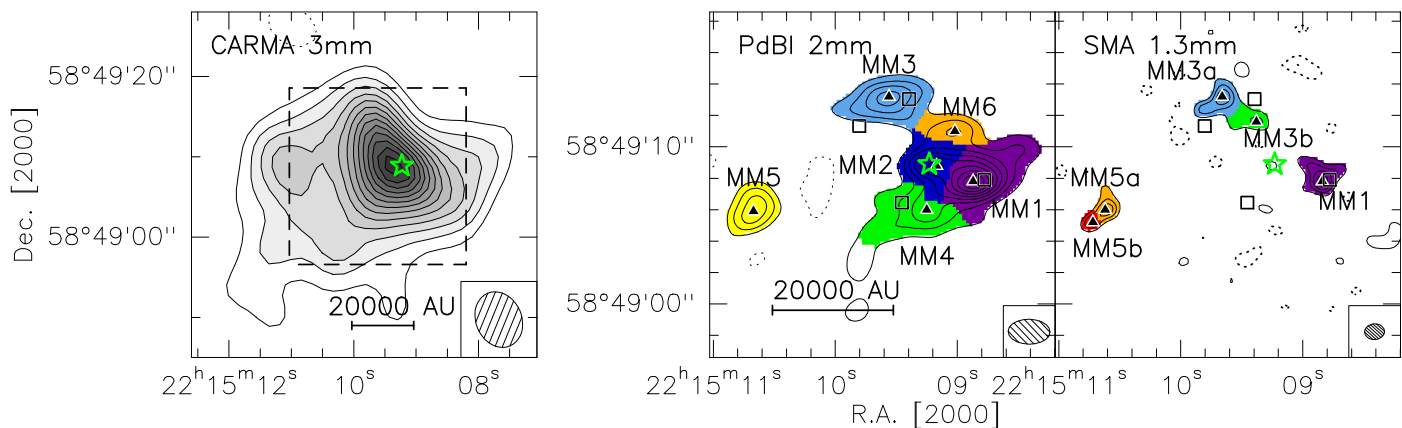


Fig. 3. The millimeter continuum map obtained with the CARMA (left), PdBI (middle) and SMA (right). Contour levels start at 3σ in steps of 2σ . The σ of the contours in each panel, *from left to right*, is 0.38, 0.26, 0.50 mJy beam $^{-1}$, respectively. The dashed box in the left panel marks the region plotted in the middle and right panel. The color-scales in the PdBI and SMA panels show the core structures and boundaries derived from the ClumpFind procedure, the triangles and the numbers mark the peaks as listed in Table 6. The star marks the UCHII region VLA1. The squares mark the cores detected by Palau et al. (2013). The dotted contours are the negative features due to the missing flux with the same contour levels as the positive ones in each panel. The synthesized beam is shown in the bottom right corner of each panel.

coupled, thus we take T_{rot} to be equaled to dust temperatures T_{dust} . In cores for which the T_{rot} measurements are not available, a dust temperature of 20 K is assumed. The results are shown in Table 6. Adopting the spectral index $\alpha = -0.19$ we derived for the centimeter emission of VLA1 in Sect. 3.1, we estimate the free-free flux at 2 mm (2.0 mJy) and 3 mm (2.2 mJy), and correct the mass and column density estimations which are listed for MM2 and the CARMA clump in Table 6. We took into account only the error from the intensity and flux measurement to estimate the error for the mass and column density estimations as listed in Table 6. The uncertainty for the T_{rot} measurements is $\sim 10 - 20\%$ (Busquet et al. 2009), which would also bring $< 30\%$ uncertainty in our mass and column density estimation.

3.3. Molecular line emission

3.3.1. Large scale

The CARMA and VLA molecular line observations are used to study the large scale structure of the molecular cloud in this region. Most of the molecular gas is concentrated at the southeast edge of the NIR cluster, and the cometary arc of the HII region VLA1 is also pointing towards this direction. Figure 5 shows that the molecular cloud traced by $\text{N}_2\text{H}^+(1-0)$ and $\text{NH}_3(1,1)$ consists of several clumps forming an extended structure around the UCHII region and the NIR cluster. Two main structures can be identified in the $\text{N}_2\text{H}^+(1-0)$ and $\text{NH}_3(1,1)$ maps, one to the southeast of the NIR cluster and the other one to the southwest. The two main structures are not associated with any embedded infrared source (Fig. 5), thus we name them high-mass starless clump east (HMSE-E) and west (HMSE-W). Several small clumps are detected in $\text{N}_2\text{H}^+(1-0)$ and $\text{NH}_3(1,1)$ maps, which are located in the north and northwest of the NIR cluster. Additionally, the $\text{NH}_3(1,1)$ emission also reveals an elongated filament extending from the southeast to the northwest across the center of the ring shape of the NIR cluster, we name it central filament (Fig. 5). Three deuterated ammonia *ortho*- NH_2D clumps are detected surrounding the NIR cluster, we name them $\text{NH}_2\text{D-N}$ (north), $\text{NH}_2\text{D-E}$ (east), and $\text{NH}_2\text{D-S}$ (south), respectively. $\text{NH}_2\text{D-N}$ is associated with $\text{NH}_3(1,1)$ and $\text{N}_2\text{H}^+(1-0)$ emission, $\text{NH}_2\text{D-S}$ is associated with the southern peak of HMSE-W, and $\text{NH}_2\text{D-E}$ sits close to the southeastern tail of the HMSE-E.

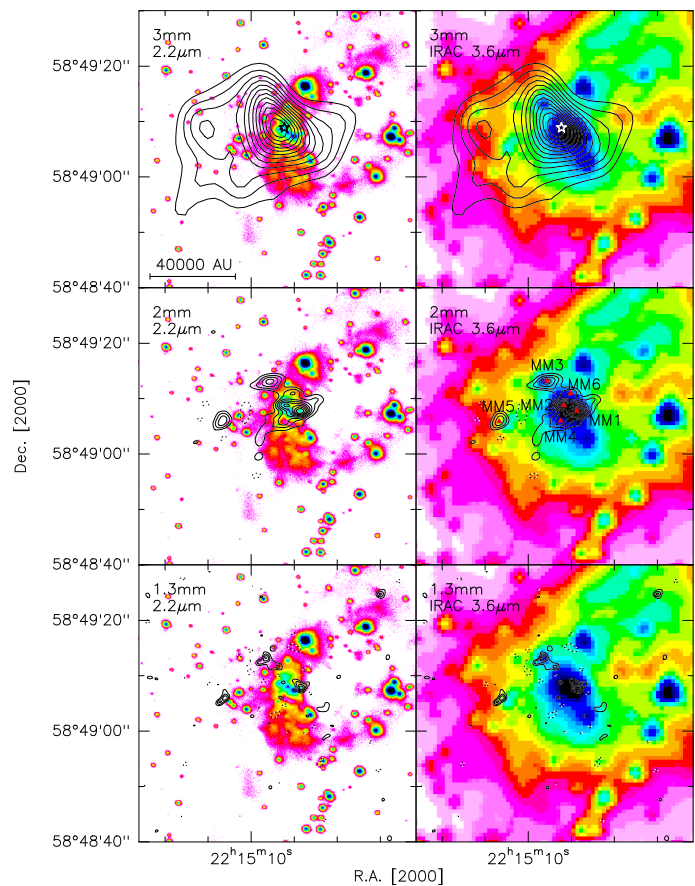


Fig. 4. The millimeter continuum map obtained with the CARMA, PdBI and SMA overlaid with UKIRT K -band ($2.2 \mu\text{m}$, left) and *Spitzer*/IRAC $3.6 \mu\text{m}$ (right) images. Contour levels start at 3σ in steps of 2σ in all panels. The stars in the top-panels mark the UCHII region VLA1. The UKIRT K -band image is from Kumar et al. (2003). The *Spitzer*/IRAC post-bcd data processed with pipeline version S18.25.0 have been downloaded from the *Spitzer* archive to create these images.

Single dish observations done by Fontani et al. (2015) detected *ortho*- NH_2D emission towards the UCHII region and HMSE-E with the same peak intensity of 0.05 K (corresponding 200 mJy

Table 6. Millimeter continuum peak properties.

Cores	R.A. (J2000)	Dec. (J2000)	I_ν^a (mJy beam ⁻¹)	S_ν^a (mJy)	Mass ^b (M_\odot)	$N_{\text{H}_2}^b$ ($\times 10^{23}$ cm ⁻²)	T_{dust} (K)	size arcsec ²
3 mm								
clump ^c	22:15:09.30	58:49:08.7	8.8±0.38	48.8± 10.4	159.5±33.9	2.3± 0.1	25 ^d	736.0
2 mm								
MM1	22:15:08.87	58:49:07.8	4.9±0.26	9.3± 2.0	6.1± 1.3	2.5± 0.1	20	20.8
MM2 ^c	22:15:09.17	58:49:08.8	1.5±0.26	2.9± 1.1	1.9± 0.7	0.8± 0.1	20	11.0
MM3	22:15:09.56	58:49:13.2	2.6±0.26	4.7± 1.1	2.2± 0.5	0.9± 0.1	27 ^d	15.3
MM4	22:15:09.25	58:49:06.0	2.2±0.26	4.4± 1.1	2.9± 0.7	1.1± 0.1	20	16.1
MM5	22:15:10.67	58:49:05.9	2.1±0.26	2.6± 0.7	1.7± 0.4	1.1± 0.1	20 ^d	8.6
MM6	22:15:09.02	58:49:11.0	1.9±0.26	2.0± 0.6	1.3± 0.4	1.0± 0.1	20	7.2
1.3 mm								
MM1	22:15:08.84	58:49:07.8	5.3±0.5	9.5± 2.2	1.5± 0.3	2.0± 0.2	20	4.9
MM3a	22:15:09.66	58:49:13.2	4.5±0.5	8.4± 2.0	0.9± 0.2	1.2± 0.1	27 ^d	4.6
MM3b	22:15:09.38	58:49:11.6	2.9±0.5	4.2± 1.2	0.5± 0.1	0.8± 0.1	25 ^d	2.9
MM5a	22:15:10.62	58:49:06.0	4.4±0.5	4.7± 1.2	0.7± 0.2	1.7± 0.2	20 ^d	2.6
MM5b	22:15:10.72	58:49:05.2	3.7±0.5	2.2± 0.7	0.3± 0.1	1.4± 0.2	20 ^d	1.2

Notes. ^(a) The errors are estimated with the same method described in the note of Table 4, and %_{uncertainty} equals to 20% for all the mm observations.

^(b) The error in the mass and column density is estimated with taking into account of the error in intensity and flux measurements only.

^(c) The results for these sources are corrected for free-free emission.

^(d) T_{dust} for these sources are derived from T_{rot} obtained from the NH₃ observations (Sect. 3.4.1), and for the rest of the sources T_{dust} is assumed to be 20 K.

with a beam size of $\sim 28''$), and this intensity is only one third of the intensity they detected towards HMSC-W. The 3σ limit for our *ortho*-NH₂D observation is ~ 273 mJy beam⁻¹ (Table 3), and larger than the peak intensity Fontani et al. (2015) detected towards the UCH_{II} region and HMSC-E. Strong C₂H($N=1-0$) and CH₃OH emission is also detected towards the southeast of the NIR cluster, and extended towards the ‘‘cavity’’ of the NIR cluster.

3.3.2. Small scale

In addition to the continuum emission, our extended configuration SMA observations also detect the CO(2–1) and SO(6₅–5₄) lines. The ¹²CO(2–1) outflow maps are shown in the left-panels of Fig. 6. The ¹²CO(2–1) spectra (right-panels, Fig. 6), which were extracted from the respect peaks of the red- and blue-shifted emission (left-panels, Fig. 6), show that most of the emission close to the v_{LSR} is filtered out by the interferometer. The ¹²CO(2–1) spectrum towards the blue-shifted emission peak shows strong blue-shifted emission but no red-shifted emission. Similarly, the spectrum extracted towards the red-south peak shows strong red-shifted emission but no blue-shifted emission. The spectrum towards the red-north peak shows weak blue-shifted emission at low velocity (-26.5 to -23 km s⁻¹), and strong red-shifted emission at both high and low velocity. The ¹²CO(2–1) outflow maps shows a bipolar outflow that is roughly in the south-north direction. The outflow maps show that the candidate driving source could be MM2, MM4 or the infrared source IRS1 suggested by Palau et al. (2013) (see Fig. 3 in Palau et al. 2013), which is marked with cross in Fig. 6. However, it seems less likely that MM2 could be powering such a collimated outflow while being in an advanced evolutionary stage where it has already cleaned up most of the surrounding gas (see Sect. 4.3 and 4.4). The red-shifted emission resembles the Hubble-law

with the increasing velocity emission at a longer from the driving source (Arce et al. 2007). Previous single dish studies also detect outflow activity with a direction of southeast (blue) -to-northwest (red) in this region (e.g., Beuther et al. 2002b; López-Sepulcre et al. 2010). With a higher angular resolution PdBI A configuration observations ($0''58 \times 0''49$), Palau et al. (2013) filter out all the large scale extended emission and resolve two outflow knots, one blue-shifted in the south and one red-shifted in the north, with the size of $\sim 1 - 2''$. These outflow knots coincide with the main south-north direction blue and red-shifted peak in our outflow map (Fig. 6). NIR narrow band observations done by Kumar et al. (2002) detected knotty, nebulous H₂ emission in the northeast direction of the red-shifted outflow component (marked with green ellipses in Fig. 6), and they claim the H₂ emission is tracing the outflows. The blue-shifted emission detected in both outflow maps in the northeastern of the region could be associated with the H₂ emission. It is clearly shown in the outflow map (Fig. 6) that the blue and red-shifted components are not lined up straightly, which might be due to the inhomogeneous distribution of the ambient molecular gas or to the strong influence of the cluster and nearby stars as suggested by Kumar et al. (2002). Besides the main south-north outflow, the outflow maps also show many other red and blue-shifted lobes spread through the image, which could be due to the fact that this outflow is extended and we filter out a lot of the large scale structure, or multiple outflows driven by different sources. Multi-configuration observations as well a complementing short spacing single-dish data, in order to have a good *uv*-coverage, are necessary to understand the outflow emission structure in this region. We combined the low and high velocity outflow emission, and estimated the mass M_{out} , momentum p_{out} and energy E_{out} of the bipolar outflow which is in the south-north direction (outflow lobes marked with squares in Fig. 6). For the calculations, we applied the method of Cabrit & Bertout (1990, 1992),

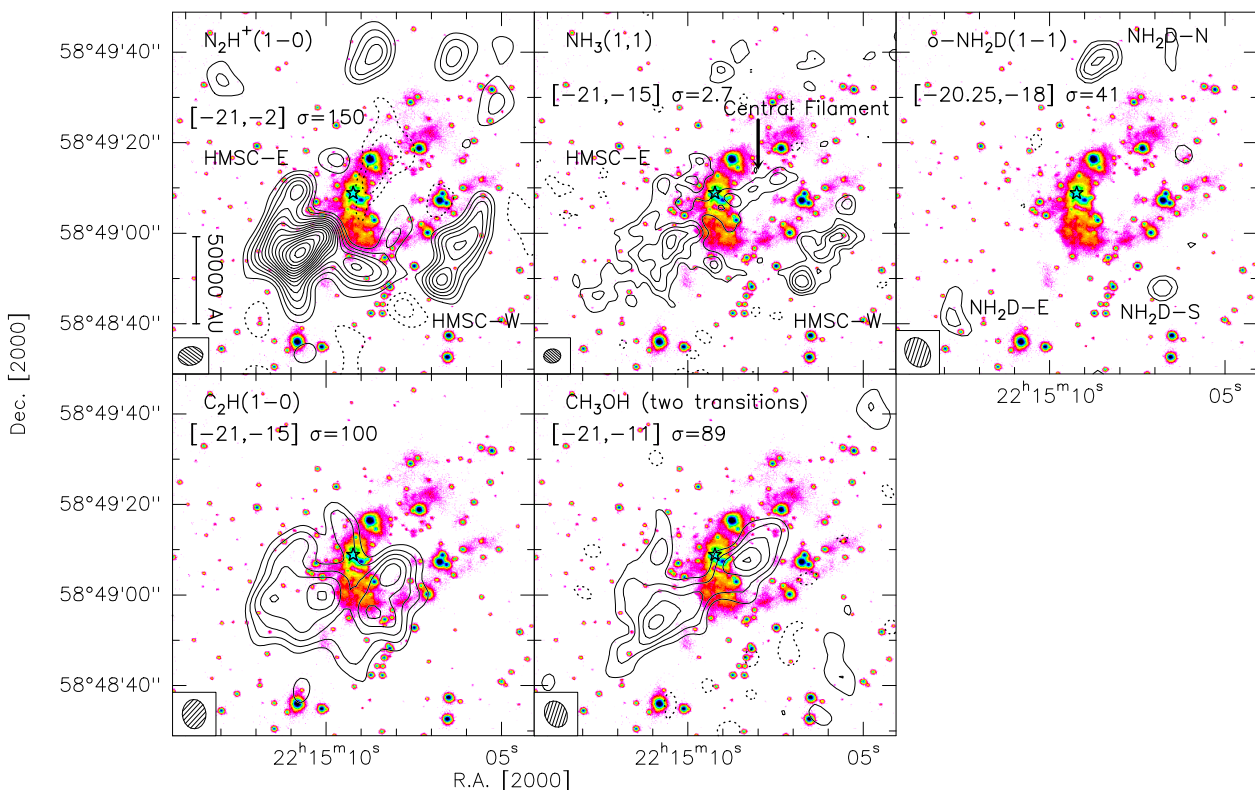


Fig. 5. The UKIRT K -band image and large scale molecular line integrated intensity maps. The contour levels start at 3σ and increase with a step of 2σ /level in all panels. The σ value and the integrated velocity ranges of each transition are shown in the respect map in the units of $\text{mJy beam}^{-1} \text{ km s}^{-1}$ and km s^{-1} , respectively. As the integrated velocity ranges show, we include all the hyperfine components $\text{N}_2\text{H}^+(1-0)$ for the integrated intensity map, for $\text{NH}_3(1, 1)$ we integrate only the main group of hyperfine components. The star marks the UCHII region, and the crosses mark the ring-shaped cluster of infrared sources identified by Kumar et al. (2003). The dotted contours are the negative features due to the missing flux with the same contour levels as the positive ones in each panel. The synthesized beam is shown in the bottom left corner of each panel.

assuming that $^{13}\text{CO}(2-1)/^{12}\text{CO}(2-1)$ line wing ratio is 0.1 (Choi et al. 1993; Beuther et al. 2002b), and $\text{H}_2/^{13}\text{CO} = 89 \times 10^4$ (Cabrit & Bertout 1992) and $T_{\text{ex}} = 30 \text{ K}$. For the blue shifted emission we derived $M_{\text{out}} \sim 0.07 M_{\odot}$, $p_{\text{out}} \sim 0.85 M_{\odot} \text{ km s}^{-1}$, and for the red shifted emission $M_{\text{out}} \sim 0.11 M_{\odot}$ and $p_{\text{out}} \sim 1.52 M_{\odot} \text{ km s}^{-1}$. The total energy of the outflow $E_{\text{out}} \sim 3.24 \times 10^{44} \text{ erg}$ (corresponding to $16.29 M_{\odot} (\text{km s}^{-1})^2$). From single-dish measurements, Beuther et al. (2002b) derived that the total outflow mass $M_{\text{out}} = 17 M_{\odot}$, total outflow momentum $p_{\text{out}} = 242 M_{\odot} \text{ km s}^{-1}$, and $E_{\text{out}} = 3.4 \times 10^{46} \text{ erg}$, which indicates that we only recovered $\sim 1\%$ of the outflow emission.

The integrated intensity map of $\text{SO}(6_5 - 5_4)$ (left-panel, Fig. 7) shows one emission peak at the continuum source MM1 and another peak in the position of R.A. $\sim 22^{\text{h}}15^{\text{m}}09^{\text{s}}.7$ Dec. $\sim +58^{\circ}49'03''$ (J2000), which could be tracing part of the large scale molecular cloud surrounding the NIR cluster (Fig. 5), and is mostly filtered out by the extended configuration SMA observations.

Figure 7 and 8 show the integrated intensity map of $\text{N}_2\text{D}^+(2-1)$. Three N_2D^+ cores are detected with a peak intensity $\geq 4\sigma$, we name these cores $\text{N}_2\text{D}^+\text{-E}$ (east), $\text{N}_2\text{D}^+\text{-C}$ (center), and $\text{N}_2\text{D}^+\text{-W}$ (west), respectively. $\text{N}_2\text{D}^+\text{-E}$ is associated with HMSC-E with strong N_2H^+ emission, and the other two N_2D^+ cores lie very close to the continuum cores and the UCHII region VLA1 and have no N_2H^+ emission (left panel, Fig. 8). It is worth noting that $\text{N}_2\text{D}^+\text{-C}$ and $\text{N}_2\text{D}^+\text{-W}$ lie just between the NH_3 peaks, this anti-correlation may indicate some peculiar chemical process. The non-detection of N_2H^+ emission towards the other two N_2D^+ cores might be due to a sensitivity issue, the rms of

N_2D^+ observations being about 20% of the rms for N_2H^+ observations (Table 3). The $\text{NH}_3(1, 1)$ filament that the N_2D^+ cores are associated with is observed with the VLA and also has a much better sensitivity and uv -coverage than the N_2H^+ observations (Table 3). Still these are the closest N_2D^+ cores to an UCHII region detected so far (projected distance $\sim 8,000 \text{ AU}$ at $d = 2.6 \text{ kpc}$). With a primary beam size of $\sim 32''$ at 2 mm , our PdBI observations can only cover HMSC-E and the UCHII region but not HMSC-W, so we do not have N_2D^+ for HMSC-W.

3.4. Analysis

3.4.1. Column density and temperature of NH_3 and N_2H^+

$\text{NH}_3(1, 1)$, $(2, 2)$ and $\text{N}_2\text{H}^+(1-0)$ emission are used to study the column density and temperature properties of the molecular cloud clumps. To compare with the N_2H^+ results, we first convolved the $\text{NH}_3(1, 1)$ and $(2, 2)$ data cube to the same angular resolution as the $\text{N}_2\text{H}^+(1-0)$ one, $5''.49 \times 4''.09$, P.A. = -82° . Then we extracted the spectra of $\text{NH}_3(1, 1)$ and $(2, 2)$ lines for positions in a grid of $0''.7 \times 0''.7$, and fitted the hyperfine structure of the $\text{NH}_3(1, 1)$ transition, and a Gaussian profile to the $\text{NH}_3(2, 2)$ using CLASS. Following the procedure described in Busquet et al. (2009), we derived the rotational temperature, and the column density maps of the NH_3 emission. For $\text{N}_2\text{H}^+(1-0)$ transition, we also extracted spectra towards each position and fitted the hyperfine structure of each line (Caselli et al. 1995), and following the procedure outlined in the appendix in Caselli

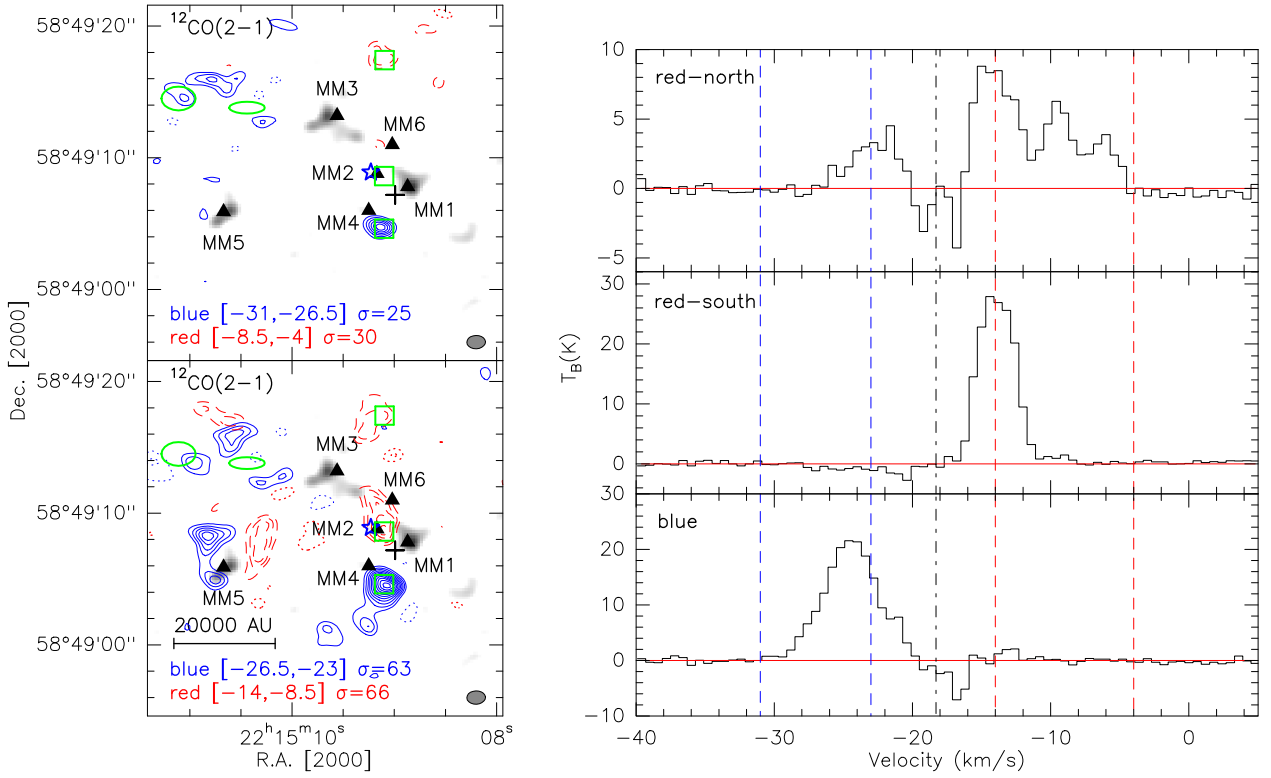


Fig. 6. The SMA $^{12}\text{CO}(2-1)$ outflow maps overlaid with the SMA 1.3 mm continuum map (*left*), and the average $^{12}\text{CO}(2-1)$ spectra extracted from the peaks of the red- and blue-shifted emission marked with squares in the *left* panels. *Top-left* panel shows the high velocity outflow map and the *bottom-left* one shows the low velocity outflow map. In both panels, the full and dashed contours show the blue-shifted and red-shifted $^{12}\text{CO}(2-1)$ outflow emission, respectively. All the contour levels start at 4σ and increase with a step of $2\sigma/\text{level}$. The σ value and velocity-integration range of each outflow emission are shown in the bottom of the left panel in the units of mJy beam^{-1} and km s^{-1} , respectively. Two open ellipses mark the nebulous H_2 emission detected by Kumar et al. (2002). The cross marks the infrared source which was suggested by Palau et al. (2013) as the driving source of the outflow. The triangles mark the positions of our 2 mm cores. The dotted contours are the negative features due to the missing flux with the same contour levels as the positive ones in the panel. The synthesized beam of the outflow map is shown in the bottom right corner of the left panel. The squares at the peaks of the red and blue outflow lobes with the size of $1''.4 \times 1''.4$ mark the area where we extracted the spectra shown in the *right* panels. In the *right* panels, the dashed lines mark the velocity regimes we used to define the outflow emission, the dashed-dotted line marks the $v_{\text{LSR}} = -18.3 \text{ km s}^{-1}$.

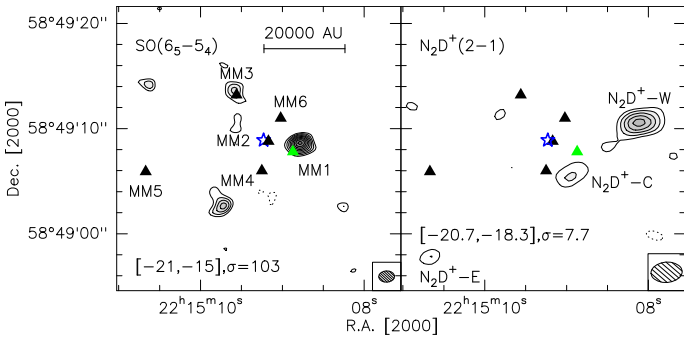


Fig. 7. The SMA $\text{SO}(6-5)$ and PdBI $\text{N}_2\text{D}^+(2-1)$ integrated intensity maps. Contour levels start at 3σ and increase with a step of 1σ . The σ value and the integrated velocity ranges of each transition are shown in the respect map in the units of $\text{mJy beam}^{-1} \text{ km s}^{-1}$ and km s^{-1} , respectively. The star marks the UCHII region, the triangles mark the 2 mm continuum sources. The dotted contours are the negative features due to the missing flux with the same contour levels as the positive ones in each panel. The synthesized beam is shown in the bottom right corner of each panel.

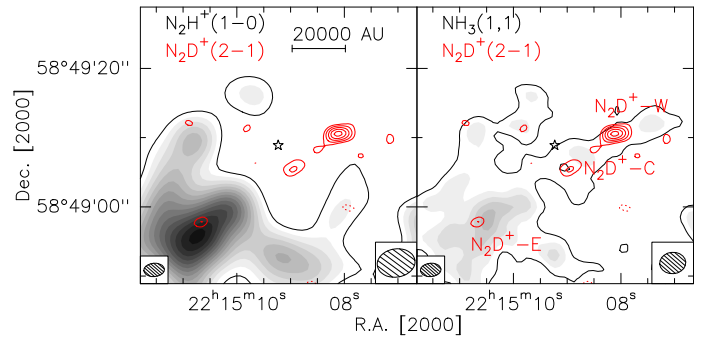


Fig. 8. $\text{N}_2\text{D}^+(2-1)$ integrated intensity map overlaid on the $\text{N}_2\text{H}^+(1-0)$ and $\text{NH}_3(1,1)$ integrated intensity maps. The contour level parameters of $\text{N}_2\text{D}^+(2-1)$ integrated intensity map are the same as in Fig. 7. The thin black contour in each panel indicate the 3σ level of the $\text{N}_2\text{H}^+(1-0)$ and $\text{NH}_3(1,1)$ integrated intensity emission. The σ values and integrated velocity range are the same as in Fig. 7 and 5, respectively. The star marks the UCHII region. The dotted contours are the negative features due to the missing flux with the same contour levels as the positive ones in each panel. The synthesized beam of $\text{N}_2\text{D}^+(2-1)$ is shown in the bottom left corner of each panel, and the one of $\text{N}_2\text{H}^+(1-0)$ and $\text{NH}_3(1,1)$ is shown in the bottom right corner of respect panel.

et al. (2002b) we derived the excitation temperature and column density maps of N_2H^+ emission. The parameters of the molecule for the calculations are obtained from CDMS (Müller et al. 2001, 2005). The resulting maps are shown in Fig. 9. While the peak

NH_3 column density for HMSC-E is $\sim 5 \times 10^{14} \text{ cm}^{-2}$, the gas close to the UCHII region shows a lower NH_3 column density

Table 7. Deuterium fraction of N_2H^+ and NH_3 .

Cores	D_{frac}
$\text{N}_2\text{D}^+\text{-E}$	0.0035
$\text{N}_2\text{D}^+\text{-C}$	0.035*
$\text{N}_2\text{D}^+\text{-W}$	0.048*
$\text{NH}_2\text{D-E}$	0.040
$\text{NH}_2\text{D-S}$	0.012
$\text{NH}_2\text{D-N}$	0.014

Notes. (*) Lower limit.

of $\sim 1 \times 10^{14} \text{ cm}^{-2}$. The NH_3 column density reaches its highest value in the western clump HMSC-W of $\sim 1 \times 10^{15} \text{ cm}^{-2}$. In contrast to the NH_3 emission, the column density of N_2H^+ peaks close to the $\text{NH}_3(1, 1)$ integrated intensity peak, with a value of $\sim 6 \times 10^{13} \text{ cm}^{-2}$, and the western clump HMSC-W has only a peak column density of $\sim 2 \times 10^{13} \text{ cm}^{-2}$. Concerning the temperature, the T_{rot} map derived from NH_3 observations shows the main part of HMSC-E has a temperature of ~ 20 to 25 K, and achieve the highest value of 30 K at the position close to the UCHII region. The western clump HMSC-W has a much lower T_{rot} of ~ 14 K. These results are consistent with the values reported in Sánchez-Monge et al. (2013), that the temperature increases when approaching the UV-radiation source. For the N_2H^+ observations, the excitation temperature T_{ex} also shows a higher temperature at position close to the UCHII region of ~ 17 K and a lower value towards HMSC-W of ~ 10 K.

The deuterated fraction (hereafter D_{frac}) of N_2H^+ , defined as the column density ratio of the species containing deuterium to its counterpart containing hydrogen, is reported to be anti-correlated with the evolutionary stages of the high-mass cores (Fontani et al. 2011). Following the procedure outlined in the appendix in Caselli et al. (2002b), we also estimate the column density of N_2D^+ and NH_2D , and then derive $D_{\text{frac}}(\text{N}_2\text{H}^+)$ and $D_{\text{frac}}(\text{NH}_3)$. The results of $D_{\text{frac}}(\text{N}_2\text{H}^+)$ and $D_{\text{frac}}(\text{NH}_3)$ are listed in Table 7. N_2H^+ 3σ upper limit is used to estimate $D_{\text{frac}}(\text{N}_2\text{H}^+)$ of the two N_2D^+ cores close to the UCHII. For simplicity, we assumed $T_{\text{ex}} = 20$ K and a beam filling factor of 1. Every 10 K change from T_{ex} would bring $< 22\%$ to our estimation for D_{frac} .

3.4.2. Kinematics

To study the kinematic properties of the molecular cloud clumps, we construct velocity maps of $\text{C}_2\text{H}(N=1-0)$, $\text{CH}_3\text{OH}(2_{0,2} - 1_{0,1})\text{A}+$, $\text{NH}_3(1, 1)$ and $\text{N}_2\text{H}^+(1-0)$ with the same spatial and velocity resolution. We convolved all the data cubes to the same spatial ($6''.49 \times 5''.23$, P.A. = 22.21°) and velocity resolution (0.42 km s^{-1}) in order to compare the velocity structure among these tracers. Single velocity component hyperfine structure fitting for $\text{NH}_3(1, 1)$ (Busquet et al. 2009) and $\text{N}_2\text{H}^+(1-0)$ (Caselli et al. 1995) are performed towards each point and produce the velocity map. For CH_3OH , the emission close to the UCHII also shows a double peaked velocity structure, and the rest part shows only one velocity component. The signal-to-noise ratio of the $\text{CH}_3\text{OH}(2_{0,2} - 1_{0,1})\text{A}+$ is not good enough to perform the multi-component fit, so we performed one velocity Gaussian fitting. We found that the $\text{C}_2\text{H}(N=1-0)$ spectrum shows strong double velocity peaks in some positions, so we followed the routine described by Henshaw et al. (2014) and Hacar et al. (2013) to perform a multiple components Gaussian fits. The process is as follows: we first compute an average spectrum in a square area with a size of $6''.49$ (about the size of the syn-

thesized beam), and decide whether the average spectrum has to be fitted with one or two velocity components. The fit results from the average spectrum are used as the initial guesses for all the spectra inside the square area. If one spectrum is fitted with two velocity components, we apply the following quality check: the separation of the two components must be larger than the half-width at half-maximum of the stronger component and the peak intensity of each component must be larger than 3σ (with $\sigma = 0.45 \text{ Jy beam}^{-1}$), otherwise, the spectrum is fitted with one velocity component (see Henshaw et al. 2014; Hacar et al. 2013 for the details of the fitting routine). While most of the C_2H emission can be fitted with one single velocity component, emission in the north and southwest requires of two velocity components. The blue-shifted component shows similar velocity to its adjacent emission, thus it is associated with the main emission structure. We combined the velocity map of the blue-shifted component with the one of the main emission and the resulting velocity map is shown in the top-left panel in Fig. 10 ($V_1(\text{C}_2\text{H})$). The velocity map of the red-shifted component is shown in panel $V_2(\text{C}_2\text{H})$ in Fig. 10.

All the velocity maps in Fig. 10 are presented with the same velocity range and were clipped at the 4σ level of the respective line channel map. The $V_1(\text{C}_2\text{H})$ velocity map shows a clear velocity gradient suggesting that the region close to the UCHII region and the NIR cluster is more red-shifted than the region far away from the UCHII region. The $\text{CH}_3\text{OH}(2_{0,2} - 1_{0,1})\text{A}+$ velocity map shows a more complicated velocity gradient along the filament, where the velocity of the structure shifts from -19.6 km s^{-1} to -18.9 km s^{-1} and back to -19.6 km s^{-1} again following the arrow in Fig. 10. The whole $\text{CH}_3\text{OH}(2_{0,2} - 1_{0,1})\text{A}+$ emission structure is also blue-shifted by $\sim 1 \text{ km s}^{-1}$ compared to other molecular line emission. Single velocity component hyperfine structure fitting for $\text{NH}_3(1, 1)$ (Busquet et al. 2009) and $\text{N}_2\text{H}^+(1-0)$ (Caselli et al. 1995) are performed towards each point and produce the velocity map.

The $\text{NH}_3(1,1)$ velocity map shows that the majority of the emission is at $\sim -18.7 \text{ km s}^{-1}$. Interestingly, the Central Filament in the $\text{NH}_3(1, 1)$ velocity shows blue-shifted emission from the main component by $\sim 1 \text{ km s}^{-1}$, while the southern and eastern region of HMSC-E shows red-shifted emission by $\sim 1 \text{ km s}^{-1}$. It is interesting to notice that the N_2D^+ cores show similar velocity $\sim -19.3 \text{ km s}^{-1}$ (Fig. 12), which further confirms that these N_2D^+ cores are associated with the $\text{NH}_3(1, 1)$ filament. This velocity structure of $\text{NH}_3(1, 1)$ is also reported by Sánchez-Monge et al. (2013). HMSC-E also shows similar velocity structure in the $\text{N}_2\text{H}^+(1-0)$ velocity map, that the southeastern part is red-shifted and the emission peak is blue-shifted.

The line width maps of $\text{C}_2\text{H}(N=1-0)$, $\text{CH}_3\text{OH}(2_{0,2} - 1_{0,1})\text{A}+$, $\text{NH}_3(1, 1)$ and $\text{N}_2\text{H}^+(1-0)$ are shown in Fig. 11. The line width maps of $\text{NH}_3(1, 1)$ and $\text{N}_2\text{H}^+(1-0)$ both show that the line width towards western clump HMSC-W is $\sim 0.4 \text{ km s}^{-1}$ smaller than the eastern one HMSC-E, and $\text{N}_2\text{H}^+(1-0)$ also shows a large line width ($\sim 2 \text{ km s}^{-1}$) to the southeast of HMSC-E. For $\text{C}_2\text{H}(N=1-0)$ and $\text{NH}_3(1, 1)$, most of the emission shows line widths around 1 km s^{-1} , while close to the UCHII region the line widths get larger than 2 km s^{-1} , which might be due to the feedback effects from the UCHII region. The $\text{NH}_3(1, 1)$ spectrum extracted from the joint region (approximately the size of one beam) between the Central Filament and the emission clump shows two velocity components one at $\sim -18.0 \text{ km s}^{-1}$ and the other at $\sim -19.3 \text{ km s}^{-1}$ (Fig. 12). Furthermore, the Central Filament has only one velocity component and is $\sim 1 \text{ km s}^{-1}$ blue-shifted from the main clump, these features together indicate that the Central Filament is at a slightly different plane from the main

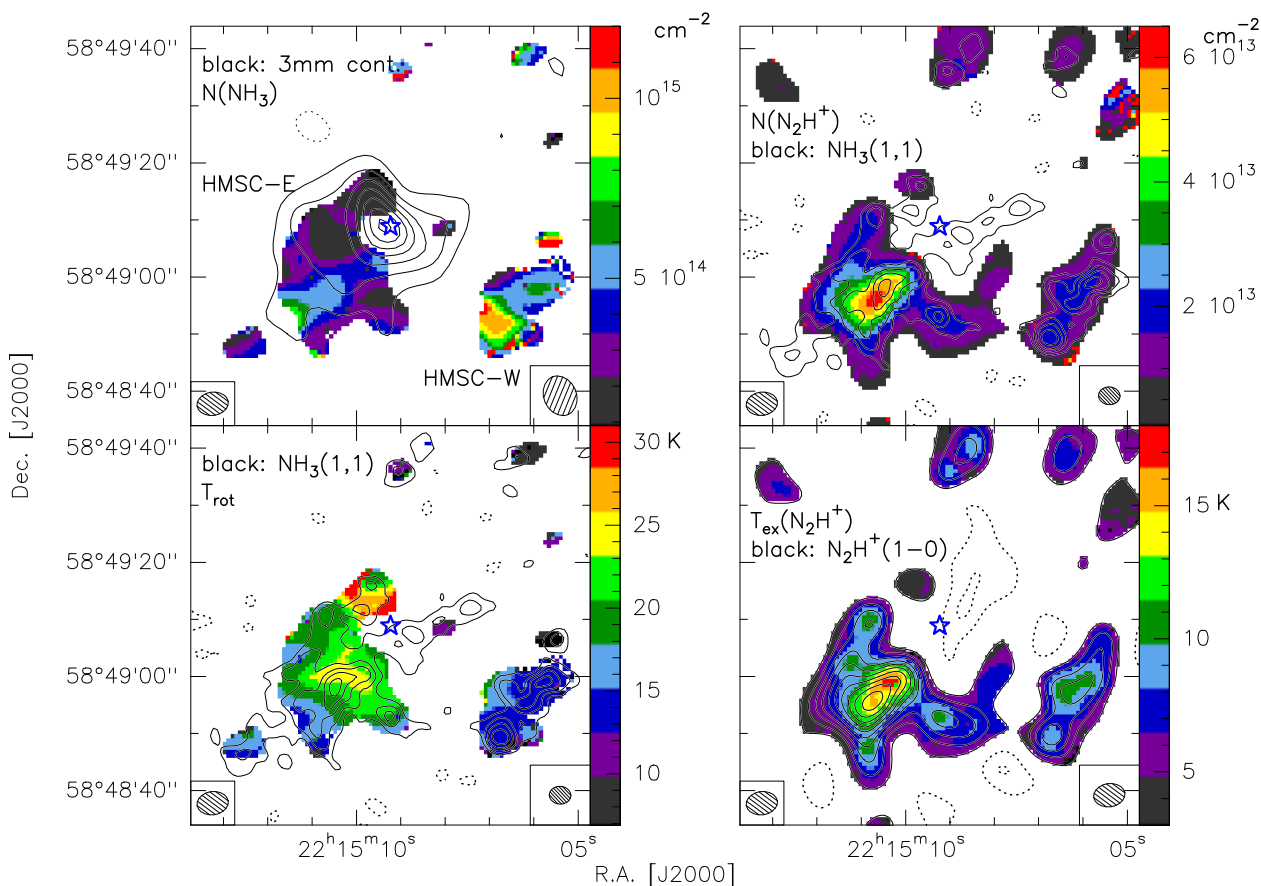


Fig. 9. *Left:* NH_3 column density map (*top*) and rotational temperature map overlaid with 3 mm continuum and $\text{NH}_3(1, 1)$ integrated intensity contours, respectively. *Right:* the N_2H^+ column density map overlaid with $\text{NH}_3(1, 1)$ integrated intensity contours (*top*), and $\text{N}_2\text{H}^+(1-0)$ excitation temperature map overlaid with $\text{N}_2\text{H}^+(1-0)$ integrated intensity contours. 3 mm continuum contours start at 3σ in steps of 4σ . All the other contour levels parameters are the same as in respect panel in Fig. 5. The synthesized beam of the temperature and column density map is shown in the bottom left corner of each panel, the synthesized beam of the contour map is shown in the bottom right corner of each panel.

clump and the NIR cluster in space. Since the N_2D^+ cores are associated with the $\text{NH}_3(1, 1)$ Central Filament, the proximity of these deuterated cores to the UCHII region could just be a projection effect. Furthermore, the Center Filament could also produce the center “cavity” seen in the NIR image (Kumar et al. 2003, see also Fig. 5) via absorbing the background emission as it is in the foreground of the cluster.

Figure 13 shows the Position-Velocity (PV) diagrams for $\text{C}_2\text{H}(N=1-0)$ and $\text{CH}_3\text{OH}(2_{0,2} - 1_{0,1})\text{A}^+$. The corresponding PV cuts of each panel are shown in Fig. 10. The PV cut marked as arrow “pv-1” in the $\text{C}_2\text{H}(N=1-0)$ velocity map cuts through the two dust continuum cores MM1 and MM3 (Fig. 10). The PV-diagram shows a “C” shape velocity structure, which indicates the C_2H emission is tracing an expanding bubble/shell structure (Arce et al. 2011). The PV cut marked as arrow “pv-2” in $\text{C}_2\text{H}(N=1-0)$ velocity map in Fig. 10 is perpendicular to the PV cut pv-1. The PV-diagram shows a clear velocity gradient with increasing velocity as we move along the PV cut pv-2, which might be indicating that the emission structure is expanding towards the observer or rotating. As C_2H is often considered as a tracer of photo-dominated regions (PDR, e.g., Millar & Freeman 1984; Jansen et al. 1995), the expanding velocity structures might be tracing the expanding PDR driven by the stellar cluster. The PV cut of $\text{CH}_3\text{OH}(2_{0,2} - 1_{0,1})\text{A}^+$ follows the CH_3OH filament (Fig. 10). The PV diagram also shows an ring shape velocity structure with the center near the UCHII region (offset 0), which is expected if the emission structure is expanding

(Arce et al. 2011). CH_3OH is well known as a shock tracer (e.g., Beuther et al. 2005; Jørgensen et al. 2004), the expanding velocity structure could be tracing the interaction front of the molecular cloud and the stellar wind from the cluster members.

We selected five typical positions, indicated in Fig. 10 by the red circles, and extracted the spectra of $\text{C}_2\text{H}(N=1-0)$, $\text{CH}_3\text{OH}(2_{0,2} - 1_{0,1})\text{A}^+$, $\text{NH}_3(1, 1)$ and $\text{N}_2\text{H}^+(1-0)$ to compare the kinematic properties in different location. Position A is chosen because it shows two velocity components in $\text{C}_2\text{H}(N=1-0)$ and large line width in $\text{NH}_3(1, 1)$ and $\text{N}_2\text{H}^+(1-0)$. Position B is close to the emission peak of $\text{NH}_3(1, 1)$ and also shows two velocity components in $\text{CH}_3\text{OH}(2_{0,2} - 1_{0,1})\text{A}^+$. Position C shows two velocity components in $\text{C}_2\text{H}(N=1-0)$ and large line width in $\text{N}_2\text{H}^+(1-0)$. Position D and E are the peak positions of $\text{N}_2\text{H}^+(1-0)$ integrated emission towards HMSC-W. We compute the average spectra within the circular area with a radius of $3''.5$ (the synthesized is $6''.49 \times 5''.23$) at each position, then single or two velocity components are fitted to the average spectra. The spectra and fitting results are shown in Fig. 14 and Table 8. In Table 8, for positions that the line was fitted with two velocity components, the red-shifted one is marked with subscript 1 (e.g., A_1) and the red-shifted one is marked with subscript 2 (e.g., A_2). While the spectra of $\text{C}_2\text{H}(N=1-0)$ at position A and C show clear double peaked features, the spectrum at position B has only one peak. Furthermore, position B is at the peak position of the integrated intensity of $\text{C}_2\text{H}(N=1-0)$ (Fig. 5), while A and C are situated at the edge of the emission structure. Thus the double

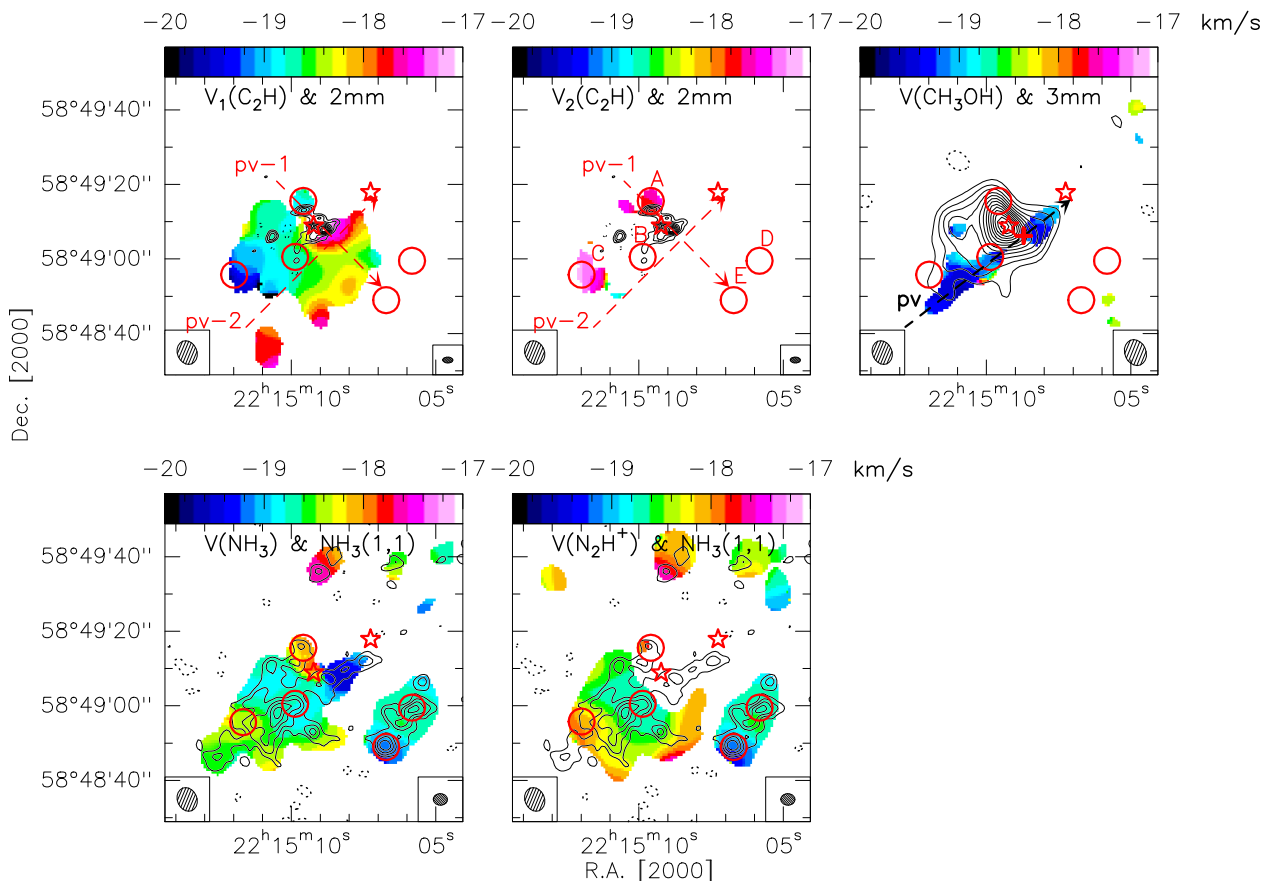


Fig. 10. Molecular line velocity maps overlaid with 2 mm, 3 mm continuum map and $\text{NH}_3(1, 1)$ integrated intensity map. The contour level parameters are the same as the ones in Fig. 3 and 5. The dashed arrows in the *top* panels mark the PV-cuts used for PV diagrams in Fig. 13. The star marks the UCHII region. The cross in the top-right panel marks the reference position in CH_3OH PV diagram in Fig. 13. The circles mark the area where the average spectra are extracted and shown in Fig. 14. The synthesized beam of the velocity maps is shown in the bottom left corner of each panel, and the one of the contours is shown in the bottom right corner of respect panel.

peaked feature at position A and C should be due to that two components coincide along the line of sight, not due to self-absorption. These two components may trace different parts of the PDR. As we mentioned above and showed in Fig. 14, two velocity components are found in $\text{CH}_3\text{OH}(2_{0,2} - 1_{0,1})A+$ line at position B, but we could not fit the spectrum properly, thus we exclude this line from the discussion below. For $\text{NH}_3(1, 1)$, we do not find double peaked features towards these five positions. All the $\text{N}_2\text{H}^+(1-0)$ spectra can be fitted with one component, except the one from position C. The isolated component of the average spectrum at position C shows a clear double peaked feature. The double peaked feature is shown in the average spectrum but very difficult to identify in each single spectrum, because the isolated component of the $\text{N}_2\text{H}^+(1-0)$ hyperfine transitions we used to determine the number of components to fit is relatively weak and double peaked feature is only shown towards the southeast edge. The red-shifted component of the $\text{N}_2\text{H}^+(1-0)$ and $\text{C}_2\text{H}(N=1-0)$ emission at this position shows similar velocity, which indicates they are associated with each other.

To estimate the contribution of the non-thermal component in the molecular emission, we assumed the relation $\sigma_{\text{nth}} = \sqrt{\sigma_{\text{obs}}^2 - \sigma_{\text{th}}^2 - \sigma_{\text{reso}}^2}$, where σ_{obs} is the measured velocity dispersion, σ_{th} is the thermal velocity dispersion, and σ_{reso} is the velocity dispersion introduced by the velocity resolution of our data. For a Gaussian line profile with the FWHM line-width Δv is obtained from the fittings, then $\sigma_{\text{obs}} = \Delta v / \sqrt{8 \ln 2}$, and

$\sigma_{\text{reso}} = 0.42 / \sqrt{8 \ln 2}$. Assuming a Maxwellian velocity distribution, σ_{th} can be calculated from $\sqrt{k_B T_k / (\mu m_H)}$, where k_B is the Boltzmann constant, μ is the molecular weight, m_H is the mass of the hydrogen atom, and T_k is the kinetic temperature. We assumed LTE conditions, so that T_{rot} obtained from NH_3 observations approximates the kinetic temperature T_k , and that T_k is the same for all molecules. The non-thermal to thermal velocity dispersion ratio $\sigma_{\text{nth}} / \sigma_{\text{th}}$ are listed in Table 8. In Table 8, we also list the Mach number $\sqrt{3} \sigma_{\text{nth}} / c_s$, where c_s is the sound speed estimated using a mean molecular weight $\mu = 2.3$.

As listed in Table 8, the ratios between $\sigma_{\text{nth}} / \sigma_{\text{th}}$ for all the lines are all above 2.3. For $\text{C}_2\text{H}(N=1-0)$ and $\text{NH}_3(1, 1)$ the non-thermal contribution to the velocity dispersion is more pronounced towards position C than A and B. For $\text{N}_2\text{H}^+(1-0)$, the $\sigma_{\text{nth}} / \sigma_{\text{th}}$ ratio towards position C is much larger than B, but comparable to A. Considering the S/N ratio for $\text{N}_2\text{H}^+(1-0)$ line towards A is not very high, we could not rule out the possibility that the spectra contain two velocity components. The spectra of $\text{NH}_3(1, 1)$ and $\text{N}_2\text{H}^+(1-0)$ show that the non-thermal contribution to the line widths towards position E is larger than towards D. For the Mach number $\sqrt{3} \sigma_{\text{nth}} / c_s$ we obtained, all of them are above 1.0. The Mach numbers for the $\text{NH}_3(1, 1)$ lines towards D and E fit the average Mach number for quiescent starless cores (Sánchez-Monge et al. 2013).

Assuming uniform density across the molecular clump, we estimate the virial mass of the starless clump HMSC-E and HMSC-W as $M_{\text{vir}} = 210 R \Delta v^2 M_{\odot}$ (MacLaren et al. 1988;

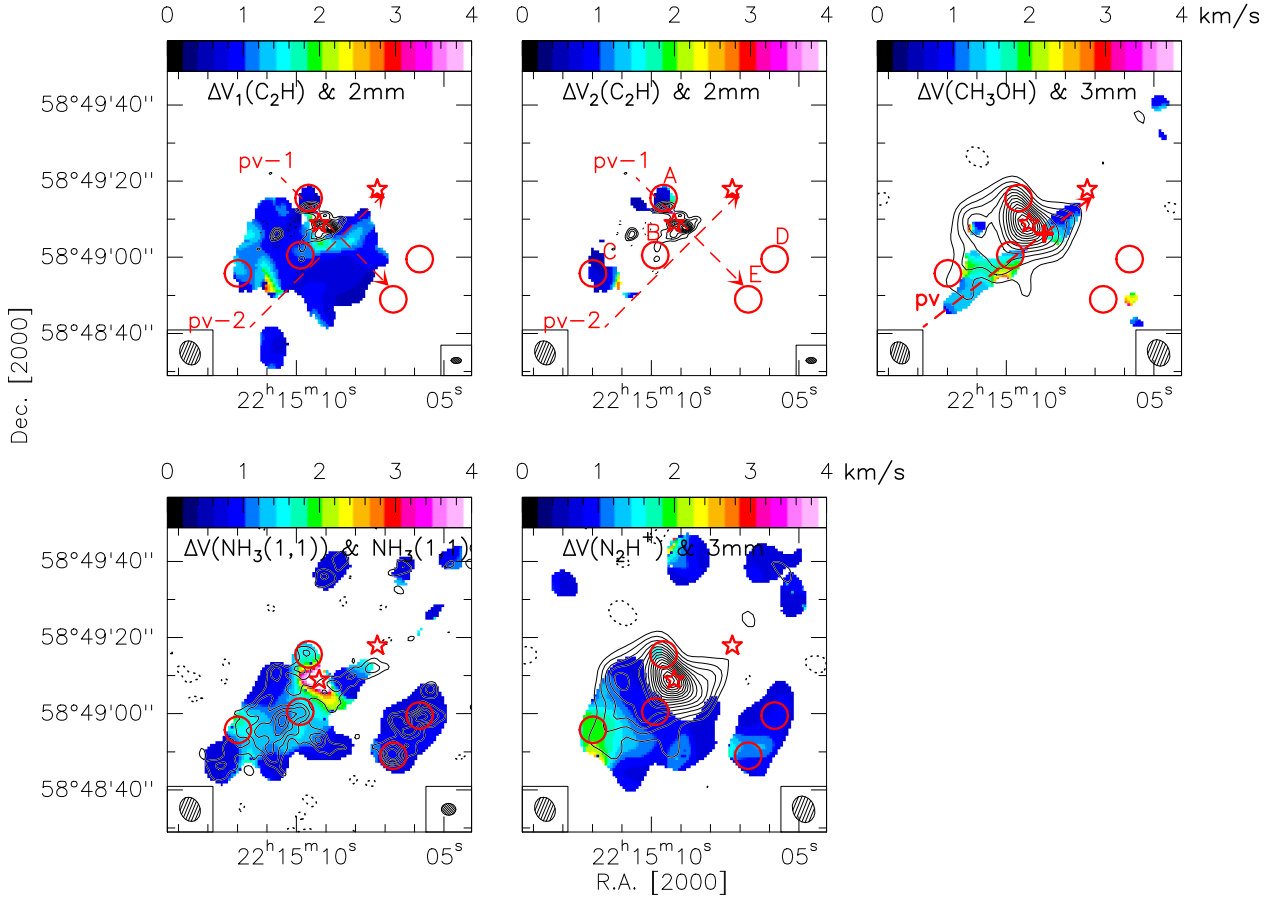


Fig. 11. Molecular line-width maps overlaid with 2 mm, 3 mm continuum map and $\text{NH}_3(1, 1)$ integrated intensity map. The contour level parameters are the same as the ones in Fig. 3 and 5. The dashed arrows in the *top* panels mark the PV-cuts used for PV diagrams in Fig. 13. The star marks the UCHII region. The cross in the top-right panel marks the reference position in CH_3OH PV diagram in Fig. 13. The circles mark the area where the average spectra are extracted and shown in Fig. 14. The synthesized beam of the line-width maps is shown in the bottom left corner of each panel, and the one of the contours is shown in the bottom right corner of respect panel.

Table 8. Fitting results of the spectral lines showed in Fig. 14.

Lines	Position	v_{peak} (km s^{-1})	Δv (km s^{-1})	σ_{nth} (km s^{-1})	$\frac{\sigma_{\text{nth}}}{\sigma_{\text{th}}}$	$\sqrt{3} \frac{\sigma_{\text{nth}}}{c_s}$
$\text{C}_2\text{H}(N=1-0)$	A ₁	-18.8	0.69	0.21	2.4	1.3
	A ₂	-17.7	0.67	0.20	2.3	1.2
	B	-18.7	1.03	0.39	4.5	2.4
	C ₁	-19.3	1.27	0.50	6.7	3.5
	C ₂	-17.3	0.68	0.21	2.9	1.5
$\text{NH}_3(1, 1)$	A	-18.2	1.52	0.61	5.7	3.6
	B	-18.8	1.40	0.53	5.0	3.2
	C	-18.4	1.44	0.58	6.3	4.1
	D	-18.7	0.76	0.26	3.1	2.0
	E	-19.1	0.87	0.31	3.9	2.5
$\text{N}_2\text{H}^+(1-0)$	A	-18.0	1.57	0.64	7.7	3.8
	B	-18.7	0.94	0.35	4.3	2.1
	C ₁	-18.6	1.30	0.52	7.4	3.6
	C ₂	-17.3	0.84	0.30	4.3	2.1
	C _s [*]	-18.1	1.92	0.79	11.4	5.6
	D	-18.7	0.82	0.29	4.6	2.3
E	-19.1	1.14	0.45	7.3	3.6	

Notes. ^(*) The results from single Gaussian component fitting.

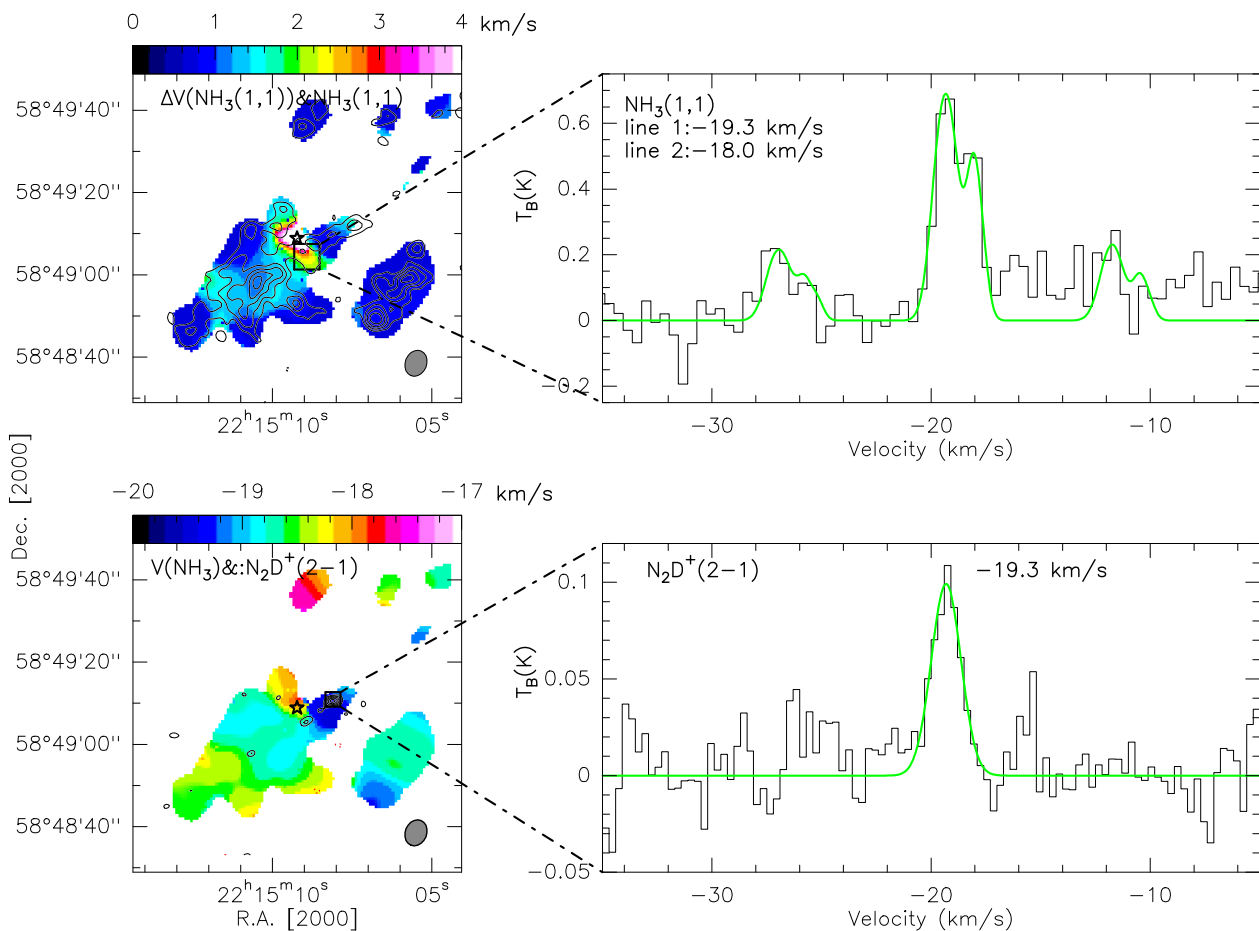


Fig. 12. *Top:* $\text{NH}_3(1,1)$ line-width map overlaid with $\text{NH}_3(1,1)$ integrated intensity map, and the average $\text{NH}_3(1,1)$ spectrum extracted from the region marked with the box in the line-width map. *Bottom:* $\text{NH}_3(1,1)$ velocity map overlaid with $\text{N}_2\text{D}^+(2-1)$ integrated intensity map, $\text{N}_2\text{D}^+(2-1)$ average spectrum extracted towards the emission peak marked with the box in the velocity map.

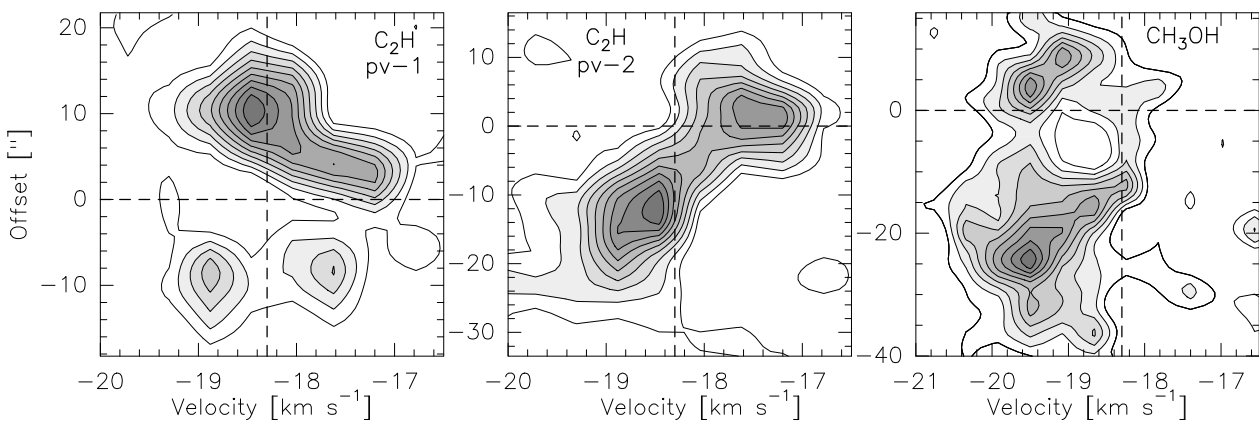


Fig. 13. Position-velocity (PV) diagrams of C_2H and CH_3OH with a velocity resolution of 0.42 km s^{-1} . The PV cuts are shown in the respect velocity map (Fig. 10). The contour levels are from 10% to 90% from the peak emission (from left to right, 0.74, 0.69, and $0.88 \text{ Jy beam}^{-1}$, respectively) in steps of 10%. The offsets refer to the distance along the cuts from the reference position, which is, from left to right, the dust continuum peak of MM1, the cross position of pv-1 and pv-2 in Fig. 10, and the cross in CH_3OH panel in Fig. 10, respectively. The v_{LSR} at -18.3 km s^{-1} and the reference position are marked by vertical and horizontal dashed lines.

Sánchez-Monge et al. 2013), where R is the radius of the main NH_3 emission structures which have the column density measurements (top-left panel, Fig. 9), and Δv is the average $\text{NH}_3(1,1)$ line width of the starless clump. The virial mass we obtained for HMSC-E is $\sim 50 M_{\odot}$ and for HMSC-W is $\sim 14 M_{\odot}$. To derive the LTE gas mass for HMSC-E and HMSC-W, first we estimated the NH_3 fractional abundance by comparing the average gas col-

umn density and the average NH_3 column density of HMSC-E. The average gas column density was determined from the 3 mm continuum map with the same area as HMSC-E shown in the NH_3 column density map in Fig. 9. To avoid the contamination from the center continuum source, we excluded the area within the Full Width 1% Maximum (similar to FWHM but at the 1% of maximum for a 2D Gaussian function) from the 3 mm con-

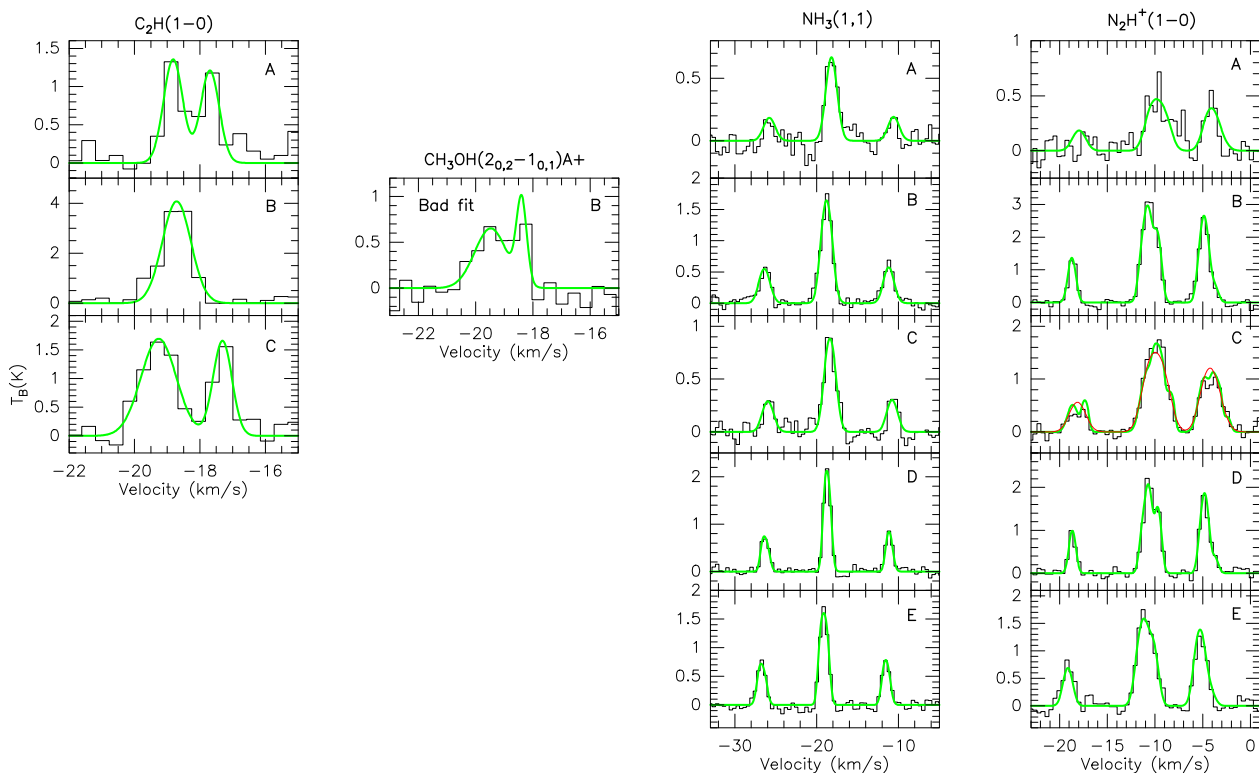


Fig. 14. Extracted spectra from the regions marked in Fig. 10 and 11. The thick lines show the fitted profile of the spectra. Gaussian fittings are performed for CH_3OH spectra and $\text{C}_2\text{H}(N=1-0)$ spectra at positions A and C with two velocity components. The spectrum of $\text{C}_2\text{H}(N=1-0)$ at position B is fitted with one velocity component. Single velocity component hyperfine structure profile fittings are done for all $\text{NH}_3(1,1)$ spectra and $\text{N}_2\text{H}^+(1-0)$ spectra except the one from position C, in which the thick green line shows the two velocity component fitting and the thin line red shows the one component fitting. The velocity of $\text{N}_2\text{H}^+(1-0)$ spectra is offset by $\sim 8 \text{ km s}^{-1}$ because the rest frequency was set at the frequency of the isolated hyperfine component ($F_1, F=0, 1 \rightarrow 1, 2$). The results from the fittings are listed in Table 8.

tium peak. We also took some random points in the area we used for the abundance estimation and estimated the local fractional abundance to estimate the error in the average fractional abundance we derived. The derived NH_3 fractional abundance is $\sim 6.3 \pm 4.0 \times 10^{-9}$. With this abundance, we derived the LTE gas mass of HMSC-E to be $\sim 62_{-24}^{+110} M_\odot$. Assuming HMSC-W and HMSC-E share the same abundance of NH_3 , we can estimate the LTE gas mass of HMSC-W to be $\sim 60_{-24}^{+100} M_\odot$. The error for the LTE mass were estimated by taking into account only the error from the NH_3 fractional abundance. The LTE masses we derived for these two clumps are larger than the virial masses, which indicates that these clumps could be gravitationally bound and will probably collapse. This also agrees with the study done by Shimoikura et al. (2013) with single-dish observations towards giant molecular clouds showing that clumps without IR clusters are mostly located below the $M_{\text{vir}}=M_{\text{LTE}}$ in the M_{vir} vs M_{LTE} plot. Previous studies show that the NH_3 fractional abundance in the cold and dense clouds is on the order of a few 10^{-9} to 10^{-7} (e.g., Tafalla et al. 2006; Pillai et al. 2006; Foster et al. 2009; Friesen et al. 2009). The low NH_3 fractional abundance we derive also suggests that the N-bearing molecules might start to be depleted, at least in the northern part of the HMSC-E clump (Aikawa et al. 2005; Flower et al. 2006; Friesen et al. 2009).

4. Discussion

4.1. The nature of the continuum cores

To compare the continuum emission at different wavelengths, we made 2 mm and 3 mm continuum images with the same range of

projected baselines (9.54–28.1 k λ), and convolved the resulting images to the same resolution of $6''.5 \times 5''.4$, P.A. = 18.5° . Similarly we also made 1.3 mm and 2 mm continuum images with the same range of projected baselines (16.00–88.88 k λ), and convolved the resulting images to the same resolution of $2''.7 \times 1''.6$, P.A. = 88° . The images are shown in Fig. 15. As we can see in the left panel of Fig. 15, the 3 mm continuum is consistent with the 2 mm one, although the 3 mm emission peak is offset by $\sim 2''$ from the 2 mm one, it is smaller than the size of the synthesized beam. The right panel in Fig. 15 shows that the 2 mm and 1.3 mm continuum images are consistent with each other. The 1.3 mm continuum emission associated with core MM1 shows extended emission towards VLA1, which is probably filtered out in the original higher spatial resolution map (right-panel, Fig. 3). With the identification level of 6σ , Palau et al. (2013) detected four continuum sources with higher angular resolution at 1.3 mm with PdBI (marked with open squares in Fig. 3 and Fig. 15). One of their cores located in the southwest is associated with MM1. The southeast core from Palau et al. (2013) locates close to our continuum core MM4 and offsets by $\sim 1''.6$ from it. The other two cores in the north could be part of our continuum core MM3.

Among the dense cores we detected at different wavelengths, MM2 is associated with the UCH II region VLA1, and extended emission at NIR wavelengths. Although the size of VLA1 (0.01 pc) fits a hyper-compact (HC) H II , the SED and the fitting results for the radio emission (Fig. 2) suggest VLA1 to be a UCH II (Churchwell 2002), which hosts an intermediate/high-mass protostellar object. Other continuum sources are located around MM2/VLA1, among which MM1 is the strongest source at both 1.3 mm and 2 mm, it is associated

with one infrared source and can only be detected in K -band and longer wavelengths, indicating the source is a deeply embedded intermediate/high-mass protostellar object. MM3a is associated with one IRAC source and shows no emission at K -band, which is considered to be an embedded intermediate- to high-mass protostellar object. All the other continuum sources, MM3b, MM4, MM5 (MM5a and MM5b) and MM6 are not associated with any infrared source, thus all these dense cores could be starless cores.

Single-dish millimeter measurements for I22134 at 1.2 mm (240 GHz) with IRAM 30 m show a peak intensity of ~ 229 mJy beam $^{-1}$ with a beam of $11''$ (Beuther et al. 2002a), and an integrated flux of 2.5 Jy. Assuming a dust emissivity index $\beta = 1.8$, that peak intensity corresponds to ~ 180 mJy beam $^{-1}$ at 1.3 mm, ~ 43 mJy beam $^{-1}$ at 2 mm and ~ 5 mJy beam $^{-1}$ at 3 mm with a beam size of $11''$. In our interferometer observations, the flux recovered within a beam of $11''$ is 20 mJy at 1.3 mm, meaning that $\sim 90\%$ of the flux is lost. Thus the masses we derive at 1.3 mm are a lower limit for the current mass of each source. At 2 mm we recover 24 mJy within a beam of $11''$ with our PdBI observations, comparing to the single dish flux (~ 43 mJy) we miss $\sim 44\%$ of the flux within the IRAM 30 m beam. However, within the PdBI main beam of $33''$ at 2 mm we only recover ~ 40 mJy, while the integrated flux reported by Beuther et al. (2002a) converts to 2 mm would be ~ 400 mJy, indicating that we are filtering out more extended emission. At 3 mm, the flux derived from our CARMA observations within the IRAM 30 m beam is 16 mJy, which is much larger than the one we estimated from the 30 m peak flux. Furthermore, the integrated flux reported by Beuther et al. (2002a) (2.5 Jy) converts to 3 mm would be ~ 56 mJy, and the 3 mm flux we recovered within the CARMA main beam of $77''$ is ~ 49 mJy, indicating we are recovering most of the central and extended emission. The larger peak flux from CARMA might be due to that we underestimated the 3 mm flux with a large β and the free-free emission contribution at 3 mm. Williams et al. (2004) found a mean β of 0.9 towards a sample of high-mass protostellar objects. If we adopt this value and take into account the free-free emission measured from our VLA observations, the peak intensity reported by Beuther et al. (2002a) would be ~ 15 mJy at 3 mm, which is similar to the 3 mm integrated flux within the IRAM 30 m beam derived from the CARMA observations. Furthermore, taking the flux measurement from Beuther et al. (2002a) into Equation 1 and assuming a dust temperature of 25 K, then the derived gas mass is $\sim 259 M_{\odot}$.

With a resolution of $0''.56 \times 0''.49$, Palau et al. (2013) recovered a flux of ~ 2.8 mJy at 1.3 mm for MM1, which is about 25% of the flux we recovered from our SMA observations, thus the gas mass we derived is several times larger than what they obtained. Considering the shortest baseline for the observations done by Palau et al. (2013) is 136 m, any structure larger than $0.9''$ would be filtered out (Palau et al. 2010), which is the reason they only recovered 25% of the flux we did.

4.2. Chemistry

4.2.1. Deuterium

Previous observations and models show that deuterium fractionations D_{frac} can be used as a good tracer of the evolutionary stages for low mass dense cores. For earlier starless cores, CO is depleted onto dust grains in cold ($T < 20$ K) and dense cores ($n \sim 10^5$ cm $^{-3}$) which would lead to an enhancement of the abundance of H_2D^+ and the deuterated molecules formed from it. As soon as the young stellar object is formed at the core centre it begins to heat its surroundings, the CO evaporates from the

dust grains and starts to destroy the deuterated species, thus D_{frac} decreases (e.g., Hatchell et al. 1998; Roberts & Millar 2000; Crapsi et al. 2005; Emprechtinger et al. 2009, N_2D^+ , NH_2D). Single pointing observations towards massive star formation regions indicate that $D_{\text{frac}}(\text{N}_2\text{H}^+)$ is high at the pre-stellar/cluster stage, and then drops as the temperature of the cores increases and the formation of the protostellar objects, similar to the low mass regions (Fontani et al. 2011; Gerner et al. 2015). On the other hand $D_{\text{frac}}(\text{NH}_3)$ does not show significant differences between different evolutionary stages in high-mass star-forming cores (Fontani et al. 2015).

We detected three NH_2D cores distributed around the NIR cluster (Fig. 5), all of them are associated with NH_3 emission with $T_{\text{rot}} \lesssim 18$ K (Fig. 9). No NH_2D emission is detected towards the main NH_3 peak of HMSC-E which could be due to the high temperature and intensive UV radiation from the NIR cluster towards this region ($\gtrsim 20$ K, Fig. 9). Both main NH_3 peaks for HMSC-W share similar temperatures, but no NH_2D emission is detected towards the northern peak, which might be due to the fact that the northern peak is closer to the NIR cluster and suffers from stronger UV radiation from the cluster members (Fig. 5 and 9). From single pointing observations, Fontani et al. (2015) obtained a $D_{\text{frac}}(\text{NH}_3)$ of 0.04 and 0.057 for HMSC-E and HMSC-W, respectively. With a beam size of $\sim 28''$, the pointing Fontani et al. (2015) performed towards HMSC-E does not cover NH_2D -E, and the pointing towards HMSC-W covers about one half of NH_2D -W. It is difficult to compare their results with ours, but the $D_{\text{frac}}(\text{NH}_3)$ that Fontani et al. (2015) obtained are in agreement with the number we derive for these three NH_2D cores within an order of magnitude. Although the $D_{\text{frac}}(\text{NH}_3)$ we derive are much higher than the $[\text{D}/\text{H}]$ interstellar abundance (the order of $\sim 10^{-5}$, Oliveira et al. 2003), they are still about one order of magnitude lower than the $D_{\text{frac}}(\text{NH}_3)$ of pre-protostellar cores derived from other interferometer observations (Busquet et al. 2010). Our results show that the NH_2D cores share similar temperatures, the one located furthest away from the NIR cluster, NH_2D -E, shows the largest $D_{\text{frac}}(\text{NH}_3)$, which indicates that the UV radiation from the NIR cluster and the UCHII region plays an important role affecting the $\text{NH}_2\text{D}/\text{NH}_3$ chemistry (Palau et al. 2007a; Busquet et al. 2010).

In contrast to the NH_2D cores, the detected N_2D^+ cores are located very close to the UCHII region and the NIR cluster, i.e. N_2D^+ -C is only at a projected distance of $\sim 8,000$ AU from the UCHII region VLA1. N_2D^+ -W and N_2D^+ -C are not associated with any N_2H^+ emission, but these two cores are well associated with the Central Filament identified in NH_3 . We have shown in Sect. 3.4.2 that the proximity of these deuterated cores to the UCHII region could just be a projection effect. $D_{\text{frac}}(\text{N}_2\text{H}^+)$ obtained from single-dish observations for HMSC-E (N_2D^+ -E) and VLA1 (N_2D^+ -C, N_2D^+ -W) are 0.023 and 0.08, respectively (Fontani et al. 2011). The average $D_{\text{frac}}(\text{N}_2\text{H}^+)$ we derive are much lower, which for the core N_2D^+ -E is ~ 0.0035 , and the lower limit of $D_{\text{frac}}(\text{N}_2\text{H}^+)$ for the N_2D^+ -W core is ~ 0.048 and ~ 0.035 for the core N_2D^+ -C (Table 7). The disagreement between the $D_{\text{frac}}(\text{N}_2\text{H}^+)$, which might be due to the fact that our N_2D^+ observations filter out much of the extended emission, as showed in Sect. 4.1 that 44% of the continuum flux was filtered out by our PdBI observations. Fontani et al. (2011) did find a higher $D_{\text{frac}}(\text{N}_2\text{H}^+)$ towards VLA1 than towards HMSC-E, which agrees with our results. All these features indicate that the relatively high D_{frac} in UCHII region VLA1 found by Fontani et al. (2011) could be just a projection effect due to the presence of nearby starless cores, not destroyed by the expansion of the ionized region, and falling inside the 30 m beam.

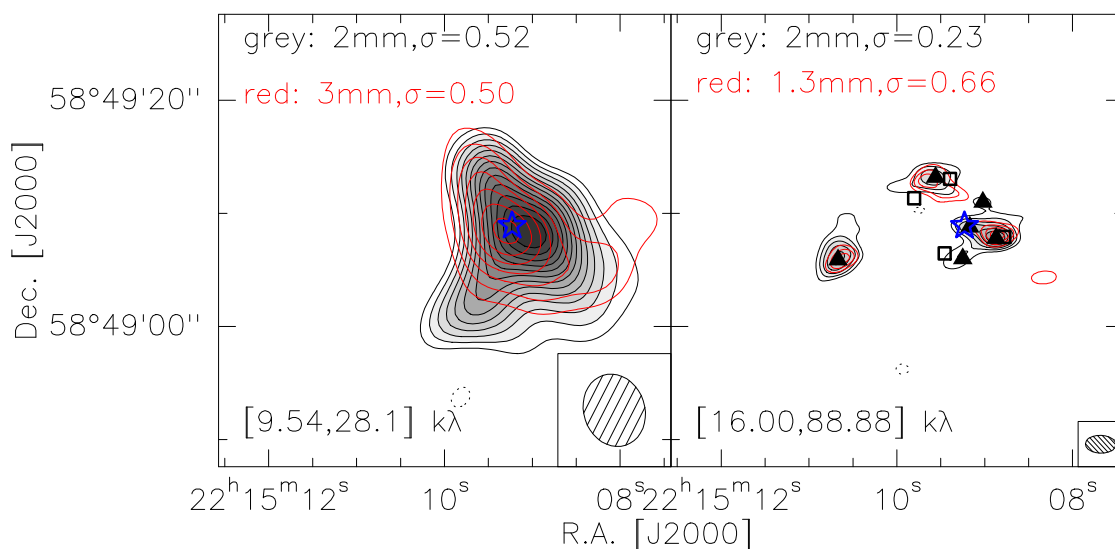


Fig. 15. The convolved mm continuum maps. *Left:* The 3 mm continuum map (red) overlaid on the 2 mm continuum map (grey scale and black contours), that both maps were produced with the same uv -range and same beam size. *Right:* The 1.3 mm continuum map (red) overlaid on the 2 mm continuum map (grey scale and black contours), that both maps were produced with the same uv -range and same beam size. The triangles mark the 2 mm cores, and the squares mark the 1.3 mm cores detected by Palau et al. (2013). The star marks the UCHII region VLA1. All the contours in both panel start at 4σ and increase with a step of 2σ . The σ value, in mJy beam $^{-1}$, and the uv -range are shown in respect panel. The dotted contours are the negative features due to the missing flux with the same contour levels as the positive ones in each panel. The synthesized beam is shown in the bottom right corner of each panel.

In the protocluster I05345, Fontani et al. (2008) detected two N_2D^+ emission structures, which are located $\sim 10,000$ AU from the nearby young B stars. These N_2D^+ emission structures extend towards a region where no N_2H^+ emission is detected above 3σ , but they are associated with NH_3 emission (Fontani et al. 2012). This could be because that the NH_3 observations in both their and our work are done with the VLA and have a much better sensitivity and uv -coverage than the N_2H^+ observations, considering the fact that the rms of our N_2H^+ observation is ≥ 20 times larger than that of the NH_3 observation, and ≥ 5 times larger than that of the N_2D^+ observation. An alternative possibility is that N_2H^+ is mostly destroyed by CO desorbed from grain mantles by heating or outflow from nearby YSOs (Busquet et al. 2011).

4.2.2. NH_3/N_2H^+ abundance ratios

While the NH_3/N_2H^+ abundance ratios that we derive for HMSC-E is ~ 15 and for HMSC-W is ~ 60 , the abundance ratios from single-dish measurements (Fontani et al. 2011, 2015) are ~ 17 and ~ 28 , respectively. Fontani et al. (2015) estimated ammonia column densities with a beam size of $\sim 32''$ and the assumed beam filling factor of 1, while the column densities of N_2H^+ were derived with a much smaller beam size ($\sim 9''$) and corrected for beam filling factor. We measured the size of HMSC-E and HMSC-W from our $NH_3(1, 1)$ integrated intensity map (Fig. 5), the equivalent diameters are $\sim 30''$ and $18''$, respectively. Thus the beam size of the ammonia by Fontani et al. (2015) is similar to the size of HMSC-E and much larger than HMSC-W, which might be the reason that the NH_3/N_2H^+ abundance ratio we derive for HMSC-E is similar to the one from Fontani et al. (2011, 2015), but the ratio for HMSC-W is much larger than the one from Fontani et al. (2011, 2015).

The NH_3/N_2H^+ abundance ratio is reported as a chemical tracer for the evolution of dense cores in low-mass star forming regions. Low-mass starless cores are reported to have NH_3/N_2H^+ abundance ratios of $\lesssim 300$, while when the YSOs form in the

center of the molecular cores, the ratio drops to $\sim 60 - 90$ (e.g., Caselli et al. 2002a; Hotzel et al. 2004; Friesen et al. 2010). A similar behaviour is found in high-mass regime, furthermore the ratio in the starless cores grows as high as $\sim 10^4$ in the starless cores (e.g., Palau et al. 2007a; Busquet et al. 2011). Furthermore, Fontani et al. (2012) and Busquet et al. (2011) proposed chemical models to explain the observed the enhancement of NH_3/N_2H^+ abundance ratio in dense starless cores. Busquet et al. (2011) suggested that in the starless stage, the CO depletion favors the formation of NH_3 against N_2H^+ , and their model showed that the abundance ratio of a collapsing core grows from ~ 0.2 to $\sim 10^4$ within 0.5 million years. HMSC-W shows higher NH_3/N_2H^+ abundance ratio than that in HMSC-E, furthermore, HMSC-W is at virial equilibrium and might be at the edge of gravitational collapsing. All these features suggest that HMSC-W might be more evolved than HMSC-E. While Table 8 shows the line width towards HMSC-W and HMSC-E are all dominated by non-thermal component, HMSC-E shows higher temperature and line width than HMSC-W (Fig. 9 and 11), which might be due to it being closer to the UCHII than HMSC-W where the feedback from UCHII is also stronger.

4.3. The expanding "bubble"

As shown in Fig. 5 and 16, N_2H^+ and NH_3 emission are distributed around the NIR cluster and follow the outline of the cluster well. The velocity structure in the $C_2H(N=1-0)$ emission suggests that the newly formed HII region VLA1 and the NIR cluster are disrupting and dispersing the natal cloud. The elongated large scale CH_3OH filament may trace the shock produced by the energetic wind which is pushing the gas away. In the left panel of Fig. 16 we marked the outline of the expanding structure with the big circle and name it as "bubble".

Zooming into the vicinity of the UCHII VLA1, Palau et al. (2013) and Sánchez-Monge et al. (2013) found that the NH_3 emission form a tilted "U" shape structure around VLA1 (right-

panel, Fig. 16). Except MM6 and MM2, the continuum cores detected in this work and Palau et al. (2013) are all distributed along the arms of the “U” shape NH₃ structure at the edges facing UCH_{II} VLA1; Furthermore, Palau et al. (2013) suggested these continuum cores could be affected by the expanding ionization front of the UCH_{II} VLA1. One arm of the “U” structure, the Central Filament, extends across the center of the ring shape NIR cluster, which is suggested to be an empty cavity by Kumar et al. (2003). Our results show that the Center Filament is in the foreground of the cluster, and the “cavity” is not empty but might be tracing the absorption from the filament (Fig. 5). We also found that NH₃(1, 1) and C₂H(*N*=1–0) show large line widths towards the “U” structure (Fig. 11), furthermore the PV-diagram pv-1 for C₂H(*N*=1–0) in Fig. 16 shows the “C” shape structure and might be tracing an expanding structure (Arce et al. 2011). All these features confirm the results from Palau et al. (2013) and the “U” structure might be tracing expansion of the UCH_{II} region VLA1.

To find out the driving source of the “bubble”, we first compare the energy of the “bubble” and the gravitational binding energy of the molecular cloud following the method outlined by Arce et al. (2011). We take the expanding velocity v_b from the C₂H(*N*=1–0) PV-diagram to be $\sim 1 - 1.5 \text{ km s}^{-1}$, the mass derived from single-dish 1 mm continuum measurements $259 M_\odot$, radius derived from N₂H⁺(1–0) integrated intensity map $\sim 40''$, 0.5 pc. Then the gravitational binding energy is estimated to be $\sim 9.5 \times 10^{45} \text{ erg}$. The kinetic energy of the “bubble” is $E_b \sim 2.6 - 5.7 \times 10^{45} \text{ erg}$, which is not enough to unbind the molecular cloud complex.

If the “bubble” is driven by stellar winds from the B1 ZAMS star, which also drives the UCH_{II} region VLA1, we can then estimate the wind mass loss rate \dot{m}_w we need to drive the “bubble” (Arce et al. 2011):

$$\dot{m}_w = \frac{P_b}{v_w \tau_w}$$

P_b is the total momentum of the “bubble” $\sim 259 - 389 M_\odot \text{ km s}^{-1}$. v_w is the wind velocity which is typically $(2 - 6) \times 10^2 \text{ km s}^{-1}$ for A and B type stars (Lamers & Cassinelli 1999; Lamers et al. 1995), we take 400 km s^{-1} . τ_w is the wind timescale $\sim 10^6 \text{ yr}$ (the duration that the wind has been active). Then \dot{m}_w is estimated to be $\sim (7 - 10) \times 10^{-7} M_\odot \text{ yr}^{-1}$. For a B1 main sequence star, assuming an effective temperature of $2.4 \times 10^4 \text{ K}$ (Gray 2005), metallicity *Z* of 1, we could derive the mass loss rate for the wind from VLA1 to be $\sim 10^{-6} M_\odot \text{ yr}^{-1}$ following the routine created by Jorick S. Vink (Vink et al. 2001, 2000, 1999). Thus VLA1 itself is already powerful enough to drive the “bubble”. The spectral type of other B stars in the cluster is $\sim \text{B3}$ (Kumar et al. 2003), and the wind from those B stars would have a mass loss rate of $\sim 10^{-6} M_\odot \text{ yr}^{-1}$. Furthermore, Figure 16 shows that VLA2 falls quite close to the geometric center of the big cavity traced by N₂H⁺ emission, therefore, we conclude that with all these B stars (Fig. 16, Kumar et al. 2003), including UCH_{II} VLA1 and VLA2, the stellar wind from the ring cluster should be strong enough to drive the “bubble”. Then the wind energy injection rate can be estimated (McKee 1989):

$$\dot{E}_w = \frac{1}{2}(\dot{m}_w v_w) v_{\text{rms}}$$

The rms velocity of the turbulent motions v_{rms} equals $\sqrt{3}\sigma_{\text{obs}}$. The average line-width for our N₂H⁺(1–0) observation is $\sim 1.0 \text{ km s}^{-1}$, which gives $v_{\text{rms}} \sim 0.74 \text{ km s}^{-1}$. We obtain that the energy ejection rate needed to drive the “bubble” is

$\dot{E}_w \sim (1.2 - 1.8) \times 10^{32} \text{ erg s}^{-1}$, which is similar to what Arce et al. (2011) found for the shells in Perseus.

Another possible driving source(s) of the “bubble” are the outflows from the YSOs, as they are considered to have strong influence on the kinematic properties of the parent clouds (e.g., Nakamura & Li 2007). The total energy of the main outflow (south-north direction) we derived in Sect. 3.3.2 is $3.24 \times 10^{44} \text{ erg}$, which is only $\sim 10\%$ of the gravitational binding energy and is not enough to unbind the molecular cloud complex. From single-dish observations, Beuther et al. (2002b) obtained the total outflow energy to be $3.4 \times 10^{46} \text{ erg}$, which should be enough to drive the “bubble”.

4.4. General picture

Combining all the kinematic properties we obtained from different molecular tracers, we propose a general picture to illustrate the star formation activity in I22134 (see Fig. 17). In the center part of I22134 sits the UCH_{II} region VLA1, radio source VLA2 and the ring shape B stars (Kumar et al. 2003) that are part of the NIR cluster. The PDR traced by C₂H(*N*=1–0) and other dense clouds traced by different molecules are distributed around the cluster. The detected mm cores are located at the edge the dense clouds facing the UCH_{II}. We propose a possible star formation scenario, that NIR cluster formed first in the same natal cloud, including the YSOs associated with the UCH_{II} regions VLA1 and VLA2. Then the expanding UCH_{II} region VLA1 created the “U” structure maybe also triggering the formation of the other mm dense cores, e.g., MM1, MM3a, around it. NIR cluster and the UCH_{II} region together are disrupting the natal cloud and HMSC-W and HMSC-E around them, may or may not be triggered.

5. Summary

The protocluster associated with I22134 represents an excellent laboratory to study the influence of massive YSOs on nearby starless cores. We have characterized the different physical and chemical properties of the dense gas by means of VLA, CARMA, PdBI and SMA observations of the centimeter and millimeter continuum, as well as several molecular tracers (NH₃, NH₂D, N₂H⁺, N₂D⁺, C₂H, CH₃OH, CO, SO). We summarize the main results below.

Multi-wavelength (E)VLA observations resolve two radio sources, VLA1 and VLA2. VLA1 is considered to be a UCH_{II} region, and shows basically constant flux at centimeter wavelengths. We can fit the SED with a homogeneous optically thin HII region with a size of 0.01 pc, and the ionizing photons flux corresponds to a B1 ZAMS star. Around the UCH_{II} region, one main clump is detected at 3 mm, 6 continuum sources are resolved at 2 mm, MM1–MM6. At 1.3 mm, MM1 has a strong counterpart, MM3 is resolved into MM3a and MM3b, and MM5 is resolved into MM5a and MM5b. MM2 is associated with the UCH_{II} region, MM1 are MM3a are associate with SO emission and NIR point sources, are considered to be intermediate to high mass protostellar objects. MM3b, MM4, MM5a, MM5b and MM6 are not associated with any NIR sources and could be starless cores. We estimated the column density and mass of each source.

At large scale, N₂H⁺(1–0) and NH₃ emission show extended structure around the UCH_{II} region and the NIR cluster, and two main structures seen in the N₂H⁺ map are considered to be starless clumps, we name them HMSC-E and HMSC-W. The rotational temperature (T_{rot}) map obtained from NH₃ observations

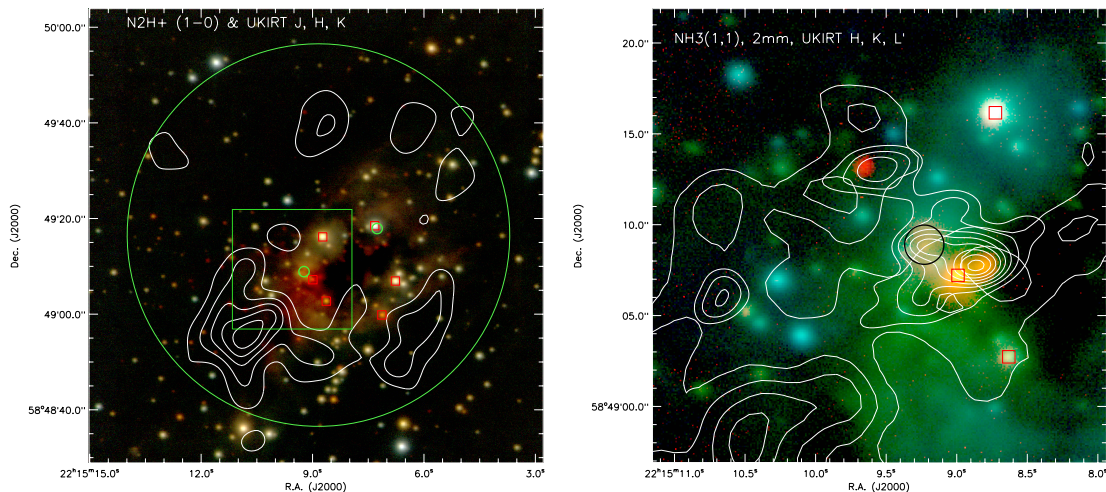


Fig. 16. *Left:* $N_2H^+(1-0)$ integrated intensity contours overlaid on J (blue), H (green), and K (red) three color image obtained from Kumar et al. (2003). Contour levels start from 3σ with 6σ per level. The big circle marks the size of the expanding bubble, the small circle in the center marks the UCHii region VLA1. The red squares mark the B stars identified by Kumar et al. (2003). *Right:* Zoom into the region marked with the green box in the *left* panel, the integrated intensity contours of the $NH_3(1, 1)$ main group of hyperfine components (thin contours), 2 mm continuum emission (thick contours) overlaid on H (blue), and K (green), and L' (red) three color image (Kumar et al. 2003). The contour level parameters are the same as in Fig. 3 and Fig. 5. The red squares mark the B stars identified by Kumar et al. (2003), and the circle marks the UCHii region VLA1.

shows higher temperature towards HMSC-E (~ 25 K) and lower towards HMSC-W (~ 15 K). HMSC-E also shows a smaller NH_3/N_2H^+ abundance ratio (~ 15) than HMSC-W (~ 60). By comparing the Virial mass and the LTE mass, we found that both HMSC-E and HMSC-W are gravitationally bound and will probably collapse. At small scale, we detected outflow from ^{12}CO emission, but the driving source for the outflow is still not clear. For the deuterium molecules, while NH_2D cores distributed around the NIR cluster and are all associated with the NH_3 emission which is at a temperature of $\lesssim 18$ K, N_2D^+ cores are associated with the NH_3 Central Filament, close to the UCHii region, with a projected distance of ~ 8000 AU ($d = 2.6$ kpc). We found that the NH_3 Central Filament is blue-shifted from the rest of the NH_3 emission by ~ 1 km s^{-1} , indicating it is at a slightly different plane from the main clump in space.

By studying the velocity map of the molecular line emission, we found the southeastern part of the $N_2H^+(1-0)$ and $NH_3(1, 1)$ emission is red-shifted from the main emission peak by ~ 1 km s^{-1} , which may indicate that the emission structure is expanding. The PV-diagram of $C_2H(N = 1 - 0)$ shows “C” shape velocity structure, which indicates the emission is tracing an expanding bubble/shell structure. We found that the “U”-shape NH_3 emission structure might be tracing the expansion of the UCHii region. We found the molecular cloud around the NIR cluster is also expanding, form a “bubble”. We estimated the stellar wind mass loss rate that is needed to produce the expanding structure, and suggest that the stellar winds from the NIR cluster are strong enough to drive the “bubble”. The outflows from the YSOs also have enough energy to dissipate the parent clouds and

drive the “bubble”. Given the kinematic properties of the molecular line emission, we propose a general picture and a sequential star formation scenario to illustrate the star formation activities in I22134.

Acknowledgements. The work is supported by the STARFORM Sinergia Project CRSII2_141880 funded by the Swiss National Science Foundation. Y.W. also acknowledges support by the NSFC 11303097 and 11203081, China. Á. S.-M. acknowledges support by the collaborative research centre project SFB 956, funded by the Deutsche Forschungsgemeinschaft (DFG). G.B. is supported by the Spanish MICINN grant AYA2011-30228-C03-01 (co-funded with FEDER funds). A.P. acknowledges financial support from UNAM-DGAPA-PAPIIT IA102815 grant, México. We thank Dr. Nanda Kumar for providing the NIR UKIRT images. We thank the productive discussion with Prof. Michael Meyer and Dr. Anastasios Fragkos. We acknowledge the referee Dr. K. Dobashi for improving the manuscript.

References

- Aikawa, Y., Herbst, E., Roberts, H., & Caselli, P. 2005, *ApJ*, 620, 330
André, P., Belloche, A., Motte, F., & Peretto, N. 2007, *A&A*, 472, 519
Arce, H. G., Borkin, M. A., Goodman, A. A., Pineda, J. E., & Beaumont, C. N. 2011, *ApJ*, 742, 105
Arce, H. G., Shepherd, D., Gueth, F., et al. 2007, *Protostars and Planets V*, 245
Beuther, H., Churchwell, E. B., McKee, C. F., & Tan, J. C. 2007, *Protostars and Planets V*, 165
Beuther, H., Schilke, P., Menten, K. M., et al. 2002a, *ApJ*, 566, 945
Beuther, H., Schilke, P., Sridharan, T. K., et al. 2002b, *A&A*, 383, 892
Beuther, H., Zhang, Q., Greenhill, L. J., et al. 2005, *ApJ*, 632, 355
Bik, A., Henning, T., Stolte, A., et al. 2012, *ApJ*, 744, 87
Bik, A., Puga, E., Waters, L. B. F. M., et al. 2010, *ApJ*, 713, 883
Busquet, G. 2010, PhD thesis, Universitat de Barcelona, Spain
Busquet, G., Estalella, R., Zhang, Q., et al. 2011, *A&A*, 525, A141
Busquet, G., Palau, A., Estalella, R., et al. 2009, *A&A*, 506, 1183

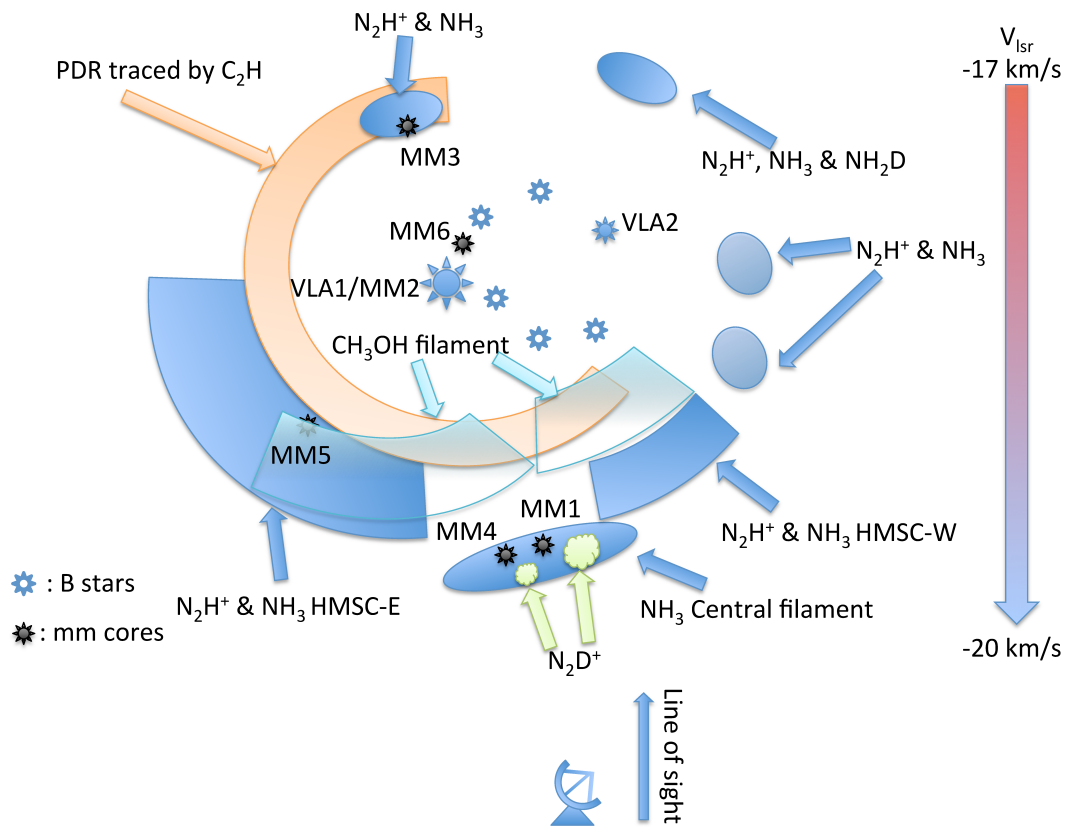


Fig. 17. The general picture of I22134 according to the kinetic properties of the molecular line observations, not scaled. The blue ellipses and block mark the dense clouds traced by different molecules as marked in the figure, the two green clouds mark the N_2D^+ cores, the orange arc shows the PDR traced by C_2H , the light blue blocks show the possible shocked emission traced by CH_3OH , the small stars mark the B stars in the cluster (Kumar et al. 2003), the big filled star marks the UCH_{II} region VLA1, the small filled star marks VLA2, the black stars mark the millimeter cores from our observations. The antenna shows our observation point.

- Busquet, G., Palau, A., Estalella, R., et al. 2010, *A&A*, 517, L6
 Cabrit, S. & Bertout, C. 1990, *ApJ*, 348, 530
 Cabrit, S. & Bertout, C. 1992, *A&A*, 261, 274
 Caselli, P., Benson, P. J., Myers, P. C., & Tafalla, M. 2002a, *ApJ*, 572, 238
 Caselli, P., Myers, P. C., & Thaddeus, P. 1995, *ApJ*, 455, L77
 Caselli, P., Walmsley, C. M., Zucconi, A., et al. 2002b, *ApJ*, 565, 344
 Chini, R., Ward-Thompson, D., Kirk, J. M., et al. 2001, *A&A*, 369, 155
 Choi, M., Evans, II, N. J., & Jaffe, D. T. 1993, *ApJ*, 417, 624
 Churchwell, E. 2002, *ARA&A*, 40, 27
 Condon, J. J., Cotton, W. D., Greisen, E. W., et al. 1998, *AJ*, 115, 1693
 Crapsi, A., Caselli, P., Walmsley, C. M., et al. 2005, *ApJ*, 619, 379
 Dobashi, K., Nozawa, S., Hayashi, Y., Sato, F., & Fukui, Y. 1994, *AJ*, 107, 2148
 Dobashi, K. & Uehara, H. 2001, *PASJ*, 53, 799
 Emprechtinger, M., Caselli, P., Volgenau, N. H., Stutzki, J., & Wiedner, M. C. 2009, *A&A*, 493, 89
 Flower, D. R., Pineau Des Forêts, G., & Walmsley, C. M. 2006, *A&A*, 456, 215
 Fontani, F., Busquet, G., Palau, A., et al. 2015, *A&A*, 575, A87
 Fontani, F., Caselli, P., Bourke, T. L., Cesaroni, R., & Brand, J. 2008, *A&A*, 477, L45
 Fontani, F., Caselli, P., Zhang, Q., et al. 2012, *A&A*, 541, A32
 Fontani, F., Palau, A., Caselli, P., et al. 2011, *A&A*, 529, L7
 Fontani, F., Zhang, Q., Caselli, P., & Bourke, T. L. 2009, *A&A*, 499, 233
 Foster, J. B., Rosolowsky, E. W., Kauffmann, J., et al. 2009, *ApJ*, 696, 298
 Friesen, R. K., Di Francesco, J., Shimajiri, Y., & Takakuwa, S. 2010, *ApJ*, 708, 1002
 Friesen, R. K., Di Francesco, J., Shirley, Y. L., & Myers, P. C. 2009, *ApJ*, 697, L457
 Gerner, T., Shirley, Y., Beuther, H., et al. 2015, *ArXiv e-prints*
 Gray, D. F. 2005, *The Observation and Analysis of Stellar Photospheres*
 Hacar, A., Tafalla, M., Kauffmann, J., & Kovács, A. 2013, *A&A*, 554, A55
 Hatchell, J., Millar, T. J., & Rodgers, S. D. 1998, *A&A*, 332, 695
 Henshaw, J. D., Caselli, P., Fontani, F., Jiménez-Serra, I., & Tan, J. C. 2014, *MNRAS*, 440, 2860
 Hildebrand, R. H. 1983, *QJRAS*, 24, 267
 Hotzel, S., Harju, J., & Walmsley, C. M. 2004, *A&A*, 415, 1065
 Jansen, D. J., van Dishoeck, E. F., Black, J. H., Spaans, M., & Sosin, C. 1995, *A&A*, 302, 223
 Jørgensen, J. K., Hogerheijde, M. R., Blake, G. A., et al. 2004, *A&A*, 415, 1021
 Kumar, M. S. N., Bachiller, R., & Davis, C. J. 2002, *ApJ*, 576, 313
 Kumar, M. S. N., Ojha, D. K., & Davis, C. J. 2003, *ApJ*, 598, 1107
 Kurtz, S. 2005, in *IAU Symposium, Vol. 227, Massive Star Birth: A Crossroads of Astrophysics*, ed. R. Cesaroni, M. Felli, E. Churchwell, & M. Walmsley, 111–119
 Lada, C. J. & Lada, E. A. 2003, *ARA&A*, 41, 57
 Lamers, H. J. G. L. M. & Cassinelli, J. P. 1999, *Introduction to Stellar Winds*
 Lamers, H. J. G. L. M., Snow, T. P., & Lindholm, D. M. 1995, *ApJ*, 455, 269
 López-Sepulcre, A., Cesaroni, R., & Walmsley, C. M. 2010, *A&A*, 517, A66
 MacLaren, I., Richardson, K. M., & Wolfendale, A. W. 1988, *ApJ*, 333, 821
 McKee, C. F. 1989, *ApJ*, 345, 782
 Millar, T. J. & Freeman, A. 1984, *MNRAS*, 207, 405
 Müller, H. S. P., Schlöder, F., Stutzki, J., & Winnewisser, G. 2005, *Journal of Molecular Structure*, 742, 215
 Müller, H. S. P., Thorwirth, S., Roth, D. A., & Winnewisser, G. 2001, *A&A*, 370, L49
 Nakamura, F. & Li, Z.-Y. 2007, *ApJ*, 662, 395
 Oliveira, C. M., Hébrard, G., Howk, J. C., et al. 2003, *ApJ*, 587, 235
 Ossenkopf, V. & Henning, T. 1994, *A&A*, 291, 943
 Palau, A., Estalella, R., Girart, J. M., et al. 2007a, *A&A*, 465, 219
 Palau, A., Estalella, R., Ho, P. T. P., Beuther, H., & Beltrán, M. T. 2007b, *A&A*, 474, 911
 Palau, A., Fuente, A., Girart, J. M., et al. 2013, *ApJ*, 762, 120
 Palau, A., Sánchez-Monge, Á., Busquet, G., et al. 2010, *A&A*, 510, A5
 Panagia, N. 1973, *AJ*, 78, 929
 Pickett, H. M., Poynter, R. L., Cohen, E. A., et al. 1998, *J. Quant. Spec. Radiat. Transf.*, 60, 883
 Pillai, T., Wyrowski, F., Carey, S. J., & Menten, K. M. 2006, *A&A*, 450, 569
 Roberts, H. & Millar, T. J. 2000, *A&A*, 361, 388
 Sánchez-Monge, Á. 2011, PhD thesis, Universitat de Barcelona, Spain
 Sánchez-Monge, Á., Palau, A., Fontani, F., et al. 2013, *MNRAS*, 432, 3288

- Sault, R. J., Teuben, P. J., & Wright, M. C. H. 1995, in *Astronomical Society of the Pacific Conference Series*, Vol. 77, *Astronomical Data Analysis Software and Systems IV*, ed. R. A. Shaw, H. E. Payne, & J. J. E. Hayes, 433–+
- Schuller, F., Menten, K. M., Contreras, Y., et al. 2009, *A&A*, 504, 415
- Scoville, N. Z., Carlstrom, J. E., Chandler, C. J., et al. 1993, *PASP*, 105, 1482
- Shimoikura, T., Dobashi, K., Saito, H., et al. 2013, *ApJ*, 768, 72
- Sridharan, T. K., Beuther, H., Schilke, P., Menten, K. M., & Wyrowski, F. 2002, *ApJ*, 566, 931
- Tafalla, M., Santiago-García, J., Myers, P. C., et al. 2006, *A&A*, 455, 577
- Tan, J. C., Beltrán, M. T., Caselli, P., et al. 2014, *Protostars and Planets VI*, 149
- Vink, J. S., de Koter, A., & Lamers, H. J. G. L. M. 1999, *A&A*, 350, 181
- Vink, J. S., de Koter, A., & Lamers, H. J. G. L. M. 2000, *A&A*, 362, 295
- Vink, J. S., de Koter, A., & Lamers, H. J. G. L. M. 2001, *A&A*, 369, 574
- Wang, Y., Beuther, H., Bik, A., et al. 2011, *A&A*, 527, A32
- Williams, J. P., de Geus, E. J., & Blitz, L. 1994, *ApJ*, 428, 693
- Williams, S. J., Fuller, G. A., & Sridharan, T. K. 2004, *A&A*, 417, 115